






# Chemical Composition of Two Bright, Extremely Metal-poor Stars from the SDSS MARVELS Pre-survey

Avrajit Bandyopadhyay<sup>1</sup> , Thirupathi Sivarani<sup>1</sup>, Antony Susmitha<sup>1</sup> , Timothy C. Beers<sup>2</sup> , Sunetra Giridhar<sup>1</sup>, Arun Surya<sup>1</sup>, and Thomas Masseron<sup>3,4</sup>

<sup>1</sup> Indian Institute of Astrophysics, Bangalore, India; [avrajit@iiap.res.in](mailto:avrajit@iiap.res.in), [sivarani@iiap.res.in](mailto:sivarani@iiap.res.in)

<sup>2</sup> Department of Physics and JINA Center for the Evolution of the Elements, University of Notre Dame, Notre Dame, IN 46656, USA

<sup>3</sup> Instituto de Astrofísica de Canarias, Vía Láctea s/n, E-38205 La Laguna, Tenerife, Spain

<sup>4</sup> Departamento de Astrofísica, Universidad de La Laguna (ULL), E-38206 La Laguna, Spain

Received 2018 February 19; revised 2018 April 9; accepted 2018 April 14; published 2018 May 30

## Abstract

SDSS J082625.70+612515.10 ( $V = 11.4$ ;  $[\text{Fe}/\text{H}] = -3.1$ ) and SDSS J134144.60+474128.90 ( $V = 12.4$ ;  $[\text{Fe}/\text{H}] = -3.2$ ) were observed with the SDSS 2.5m telescope as part of the SDSS MARVELS spectroscopic pre-survey and identified as extremely metal-poor (EMP;  $[\text{Fe}/\text{H}] < -3.0$ ) stars during the high-resolution follow-up using the Hanle Echelle Spectrograph (HESP) on the 2.0-m Himalayan Chandra Telescope. **In this paper, the first science results using HESP, we present a detailed analysis of their chemical abundances.** Both stars exhibit under-abundances in their neutron capture elements, while one of them (SDSS J134144.60+474128.90) is clearly enhanced in carbon. Lithium was also detected in this star at a level of about  $A(\text{Li}) = 1.95$ . The spectra were obtained over a span of 6–24 months, and indicate that both stars could be members of binary systems. We compare the elemental abundances derived for these two stars along with other carbon-enhanced metal-poor (CEMP) and EMP stars, in order to understand the nature of their parent supernovae. We find that CEMP-no stars and EMP-dwarfs show a very similar trend in their lithium abundances at various metallicities. We also find indications of CEMP-no stars having larger abundances of Cr and Co at given metallicities compared to EMP stars.

*Key words:* stars: abundances – stars: carbon – stars: chemically peculiar – stars: early-type – stars: neutron – stars: Population III

## 1. Introduction

Extremely metal-poor (EMP;  $[\text{Fe}/\text{H}] < -3.0$ ) stars of the Galactic halo are thought to be the immediate successors of the first stars, and were likely to have formed when the universe was only a few hundred million years old (e.g., Bromm et al. 2009); their evolution and explosion led to the first production of heavy elements. These first supernovae (SNe) had a considerable dynamical, thermal, and chemical impact on the evolution of the surrounding interstellar medium, including mini-halos that can be some distance away from the location of the first-star explosion (Cooke & Madau 2014; Smith et al. 2015; Chiaki et al. 2018). Stars (and their host galaxies) that formed thereafter are expected to carry the imprints of the nucleosynthesis events from these Population III stars (Beers & Christlieb 2005; Frebel & Norris 2015; Sharma et al. 2018). Studies of such EMP stars have greatly benefited from the large spectroscopic surveys that have been carried out in the past in order to identify them in significant numbers, such as the HK survey of Beers et al. (1985, 1992) and the Hamburg/ESO Survey of Christlieb and colleagues (Christlieb 2003). More recent surveys, such as SDSS, RAVE, APOGEE, and LAMOST continue to expand the known members of this rare class of stars (e.g., Fulbright et al. 2010; Ivezić et al. 2012; Zhao et al. 2012; Aoki et al. 2013; García Pérez et al. 2013; Anders et al. 2014; Li et al. 2015).

High-resolution spectroscopic studies of metal-poor Galactic halo stars have demonstrated diversity in their chemical compositions. For example, around 20% of stars with  $[\text{Fe}/\text{H}] < -2.0$  exhibit large enhancements in their carbon-to-iron ratios ( $[\text{C}/\text{Fe}] > +0.7$ ; Aoki et al. 2007; Lee et al. 2013, 2017). As shown by numerous studies, the frequency of carbon-enhanced

metal-poor (CEMP) stars continues to increase with decreasing  $[\text{Fe}/\text{H}]$ . The fractions of CEMP stars also increase with distance from the Galactic plane (Frebel et al. 2006; Beers et al. 2017), and also between the inner-halo and the outer-halo regions (Lee et al. 2017).

CEMP stars can be separated into four sub-classes (Beers & Christlieb 2005): (i) CEMP- $s$  stars, which show enhancements of  $s$ -process elements, (ii) CEMP- $r$  stars, which exhibit enhancements of  $r$ -process elements, (iii) CEMP- $r/s$  stars, which show enhancements in both  $r$ - and  $s$ -process elements,<sup>5</sup> and (iv) CEMP-no stars, which exhibit no neutron-capture element enhancements. Long-term radial-velocity (RV) monitoring studies have shown that most (>80%, possibly all) CEMP- $s$  stars are members of binary systems involving a (now extinct) asymptotic giant branch (AGB) star that transferred carbon and  $s$ -process rich material to the currently observed (lower-mass) star (Lucatello et al. 2005; Starkenburg et al. 2014; Hansen et al. 2016a), while CEMP-no stars exhibit observed binary frequencies typical of non-carbon-enhanced halo giants,  $\sim 18\%$  (Starkenburg et al. 2014; Hansen et al. 2016b).

Yoon et al. (2016) have considered the rich morphology of the absolute abundance of carbon,  $A(\text{C}) = \log(\text{C})$ , as a function of  $[\text{Fe}/\text{H}]$ , based on high-resolution analyses of a large sample of CEMP stars (their Figure 1, the Yoon–Beers diagram). In addition to their Group I stars, which are dominated by CEMP- $s$  stars, they demonstrate that the CEMP-no stars not only exhibit substantially lower  $A(\text{C})$ , but bifurcate into two apparently different regions of the diagram, which they refer

<sup>5</sup> Hampel et al. (2016) suggest that the observed heavy element patterns of these stars are well accounted for by an “intermediate neutron-capture process,” (as first suggested by Cowan & Rose 1977), and should be referred to henceforth as CEMP- $i$  stars.

to as Group II and Group III stars. This behavior immediately suggests that these groups might be associated with different progenitors responsible for carbon production, a suggestion borne out by the modeling carried out by Placco et al. (2016), and/or on the masses of the mini-halos in which these stars formed. Chiaki et al. (2017) have emphasized that different cooling pathways, dependent on the formation of carbon or silicate dust, may have applied to the Group III and Group II stars in the Yoon–Beers diagram.

Multiple models for the production of CEMP-no stars have been considered in the literature, such as the “spinstar” models (e.g., Meynet et al. 2006, 2010; Chiappini 2013), and the “mixing and fallback” models for faint SNe (e.g., Umeda & Nomoto 2003, 2005; Nomoto et al. 2013; Tominaga et al. 2014). Both processes may well play a role (Maeder & Meynet 2015; Choplin et al. 2016).

Regardless of the complexity of the situation, additional detailed observations of EMP stars with and without clear carbon enhancement, such as those carried out here, are required for progress in understanding. This paper is outlined as follows. In Section 2 we describe our high-resolution observations. Consideration of possible RV variations for our two targets is presented in Section 3. Section 4 summarizes our estimates of stellar atmospheric parameters, and describes our abundance analyses; the results are reported in Section 5. We present a discussion of our results with a comparative study of CEMP-no and EMP stars in Section 6, along with a brief conclusion in Section 7.

## 2. Observations and Analysis

### 2.1. Sample Selection

MARVELS (Paegert et al. 2015), a multi-object radial velocity survey designed for efficient exoplanet searches, was one of the three sub-surveys carried out as part of SDSS-III (Eisenstein et al. 2011). The targets for the first two years of MARVELS were selected based on a lower-resolution ( $R \sim 1800$ ) spectroscopic pre-survey using the SDSS spectrographs. Most of the pre-survey observations were carried out during twilight, when the fields were at low elevation. Targets were selected from these pre-survey fields for the MARVELS main radial velocity (RV) survey, which were later observed at higher elevations. There were about 30,000 stars observed as part of the spectroscopic pre-survey of stars with  $B - V > 0.6$  and  $8 < V < 13$ . Target fields for the first two years of the MARVELS survey were around known RV standards, and about 75% of the target fields were in the Galactic latitude range  $2^\circ < |b| < 30^\circ$ . Although not the ideal location to find metal-poor stars, it does offer the chance to identify a small number of bright halo targets, suitable for high-resolution spectroscopic follow-up with moderate-aperture telescopes, that happen to fall into the MARVELS pre-survey footprint during their orbits about the Galactic center. The pre-survey also has simple magnitude and color cuts, which reduces potential selection biases. As in our previously published work (Susmitha Rani et al. 2016), we used synthetic spectral fitting of the pre-survey data to identify new metal-poor candidates. Here, we present high-resolution observations and analysis of two EMP stars, SDSS J082625.70+612515.10 (hereafter SDSS J0826+6125) and SDSS J134144.60+474128.90 (hereafter SDSS J1341+4741), with  $V$  magnitudes of 11.44 and 12.38, respectively. These two stars were selected for follow

**Table 1**  
Observation Log and Radial Velocities for SDSS J0826+6125

Date	MJD	$\lambda$ Coverage (Å)	S/N	Radial Velocity (km s <sup>-1</sup> )
2015 Nov 03	57330.20903	3600–10800	51	–110.4
2015 Nov 29	57356.36042	3600–10800	49	–95.6
2015 Dec 22	57379.10417	3600–10800	47	–80.3
2016 Jan 27	57415.09792	3600–10800	47	–52.3
2016 Oct 20	57682.21667	3600–10800	50	–108.9
2016 Nov 16	57709.13542	3600–10800	51	–104.1

**Table 2**  
Observation Log and Radial Velocities for SDSS J1341+4741

Date	MJD	$\lambda$ Coverage (Å)	S/N	Radial Velocity (km s <sup>-1</sup> )
2016 Jan 27	57415.24722	3600–10800	43	–240.1
2016 Apr 24	57503.18819	3600–10800	49	–190.5
2016 Apr 26	57505.06458	3600–10800	47	–192.1
2016 Jun 24	57564.02361	3600–10800	48	–176.2
2016 Jun 25	57565.20139	3600–10800	47	–174.5

up, as they were found to be very metal poor from spectral fitting of the pre-survey data, and were also very bright. Results from the spectral fitting used to identify metal-poor candidates from the MARVELS pre-survey will be discussed in a separate paper.

### 2.2. High-resolution Observations

High-resolution ( $R \sim 30,000$ ) spectroscopic observations of the two EMP stars were obtained with the Hanle Echelle Spectrograph (HESP) on the 2.0 m Himalayan Chandra Telescope at the Indian Astronomical Observatory. The dates of observation, wavelength coverage, RVs, and signal-to-noise ratios (S/Ns) of the available spectra are listed in Tables 1 and 2.

Data reduction was carried out using the IRAF<sup>6</sup> echelle package. HESP has a dual fiber mode available, one fiber for the target star and another which can be fed with a calibration source for precise RV measurements, or by the night sky through a pinhole that has a separation of about  $13''$  from the target. The sky fiber was used for background subtraction. All the orders were normalized, corrected for RV, and merged to produce the final spectrum. The equivalent widths for individual species are listed in the tables in the Appendix. Recently, a custom data reduction pipeline has been developed by A. Surya (available publicly<sup>7</sup>) that is more suitable for the crowded and curved orders of the stellar spectra observed with HESP. However, in the present paper, we used IRAF, and proper care was taken to avoid drift of the spectral tracings blending into adjacent orders.

## 3. Radial Velocities

The HESP instrument is thermally controlled to  $\Delta T = \pm 0.1^\circ\text{C}$  at a set point of  $16^\circ\text{C}$  over the entire year, which is expected to provide a long-term stability of  $\sim 200 \text{ m s}^{-1}$  (T. Sivarani et al. 2018, in preparation), substantially lowering systematic errors with respect to a spectrograph that does not have such control.

<sup>6</sup> IRAF is distributed by the National Optical Astronomy Observatory, which is operated by the Association of Universities for Research in Astronomy (AURA) under cooperative agreement with the National Science Foundation.

<sup>7</sup> <https://www.iiaa.res.in/hesp/>

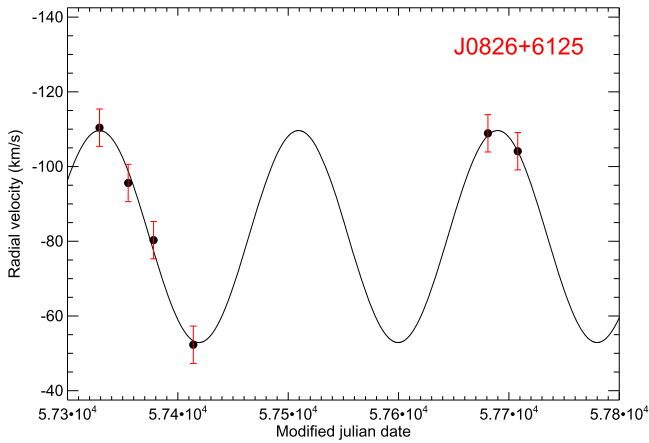


**Figure 1.** Variation of radial velocity for SDSS J0826+6125. The derived period is 180.4 days

RVs were calculated for SDSS J0826+6125 based on six epochs of observations spread over a period of 12 months. For SDSS J1341+4741, we obtained five observations spread over six months. A cross-correlation analysis was performed with a synthetic template spectrum suitable for each star to obtain the RV measurement for each spectrum. We made use of the software package RVLIN provided by Wright & Howard (2009), which is a set of IDL routines used to fit Keplerian orbits to derive the orbital parameters from the RV data. The RV measurements exhibit peak-to-peak variations of  $\sim 60 \text{ km s}^{-1}$ , with a period of 180 days for SDSS J0826+6125, and  $\sim 110 \text{ km s}^{-1}$ , with a period of 116 days for SDSS J1341+4741. The best-fit orbits for these stars, based on the data in hand, are shown in Figures 1 and 2. Although the existence of RV variations is secure, with such sparse coverage of the proposed orbits more data are required to confirm the periods.

#### 4. Stellar Parameters

Both photometric and spectroscopic data were used to derive estimates of the stellar parameters for our program stars. The effective temperatures were determined using various photometric observations in the literature and the  $T_{\text{eff}}$ -color relations derived by Ramírez & Meléndez (2005). They were found to be in close proximity (a difference of 40 K was found) to values obtained by Alonso et al. (1996, 1999). The  $V - K$  temperature estimate is expected to be superior, as it is least affected by metallicity and the possible presence of molecular carbon bands. We also employed VOSA (<http://svo2.cab.inta-csic.es/>), the online spectral energy distribution (SED) fitter (Bayo et al. 2008), to derive the temperatures using all of the available photometry (optical, 2MASS, and WISE). A Bayesian fit using the Kurucz ODFNEW/NOVER model was used to obtain the SED temperature. Final fits for the two stars are shown in Figures 3 and 4.

$T_{\text{eff}}$  estimates were also derived spectroscopically, by demanding that there be no trend of Fe I line abundances with excitation potential (shown in the upper panels of Figures 5 and 6), as well by fitting the  $H_{\alpha}$  profiles. Estimates for the effective temperatures of our target stars are listed in Table 3. For SDSS J1341+4741, we adopted the temperature obtained from fitting the  $H_{\alpha}$  wings, as this is highly sensitive to small variations in temperature. For SDSS J0826+6125, the  $H_{\alpha}$  profile was asymmetric, and thus it could not be used for

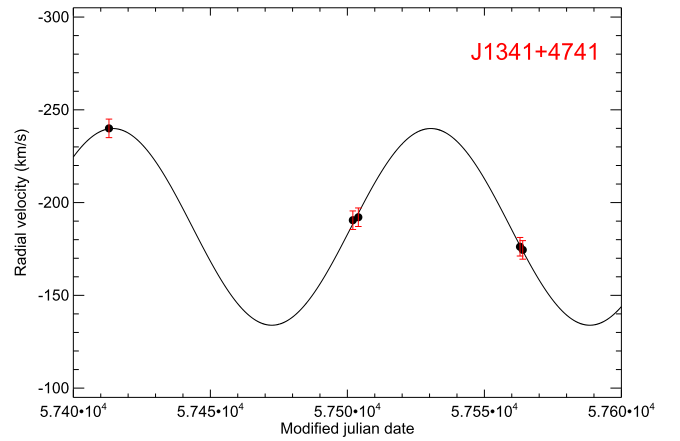


**Figure 2.** Variation of radial velocity for SDSS J1341+4741. The derived period is 116.0 days.

accurate measurement of temperature. So the temperature obtained from Fe I line abundances was adopted.

Surface gravity,  $\log(g)$ , estimates for the two stars were determined by the usual technique that demands equality of the iron abundances derived for the neutral (Fe I) and singly ionized (Fe II) lines. We used seven Fe II lines and 82 Fe I lines for SDSS J0826+6125, and five Fe II lines and 49 Fe I lines for SDSS J1341+4741; best-fit models for our target stars are shown in the upper panels of Figures 5 and 6. The wings of the Mg I lines have also been fitted to obtain estimates for  $\log(g)$ ; best-fit models are shown in Figure 7.

The microturbulent velocity ( $\xi$ ) estimates for each star were derived iteratively in this process, by demanding no trend of Fe I abundances with the reduced equivalent widths, and are plotted in the lower panels of Figures 5 and 6. The final adopted stellar atmospheric parameters are listed in Table 4.

##### 4.1. Abundance Analysis

To determine the abundance estimates for the various elements present in our target stars we employed one-dimensional local thermodynamic equilibrium LTE stellar atmospheric models (ATLAS9; Castelli & Kurucz 2004) and the spectral synthesis code turbospectrum (Alvarez & Plez 1998). We measured the equivalent widths of the absorption lines present in the spectra, and considered only those lines for abundance analysis whose equivalent width is less than 120 mÅ, since they are on the linear part of the curve of growth, and are relatively insensitive to the choice of microturbulence. We measured the equivalent widths of 53 clean lines present in the spectra of SDSS J0826+6125, among which 82 are Fe I lines, and 122 clean lines for SDSS J1341+4741, among which 49 are Fe I lines. We adopted the solar abundances for each element from Asplund et al. (2009), Scott et al. (2015a, 2015b), and Grevesse et al. (2015); solar isotopic fractions were used for all the elements. Version 12 of the turbospectrum code for spectrum synthesis and abundance estimates was used for the analysis. We adopted the hyperfine splitting provided by McWilliam (1998) and solar isotopic ratios. We also used 2D MARCS models (Gustafsson et al. 2008) to derive the abundances, but no significant deviations were obtained. The abundances differed by values ranging from 0.01 to 0.02 dex for individual species.

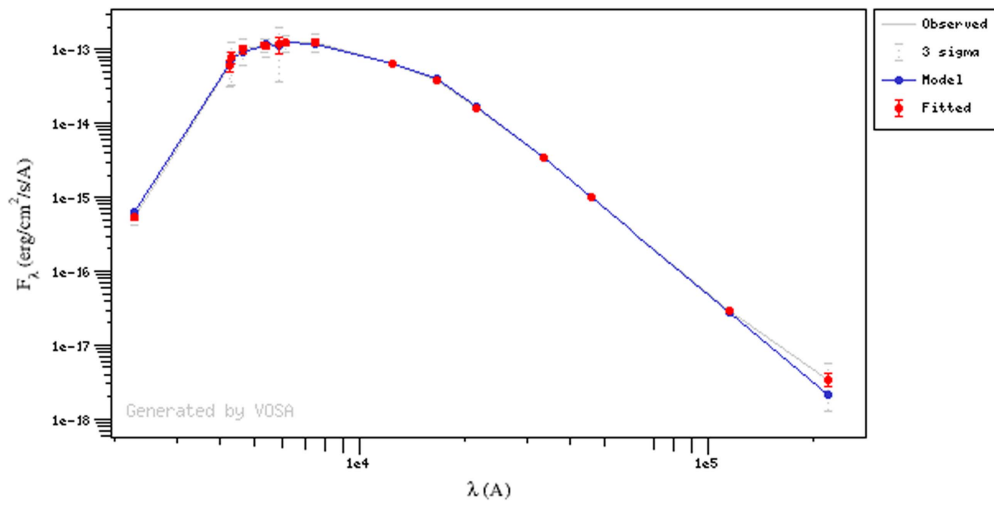


Figure 3. Spectral energy distribution obtained from VOSA for SDSS J0826+6125 showing the temperature to be  $\sim 4500$  K.

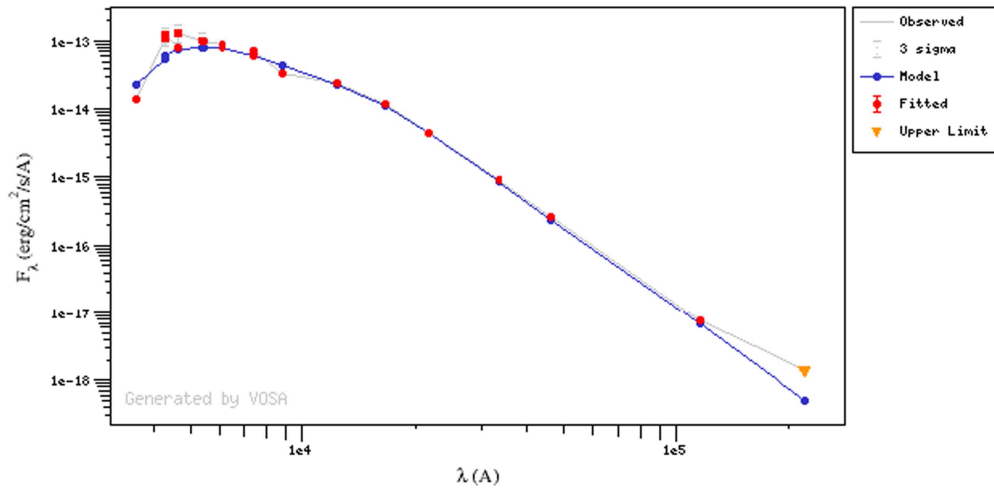


Figure 4. Spectral energy distribution obtained from VOSA for SDSS J1341+4741 showing the temperature to be  $\sim 5500$  K.

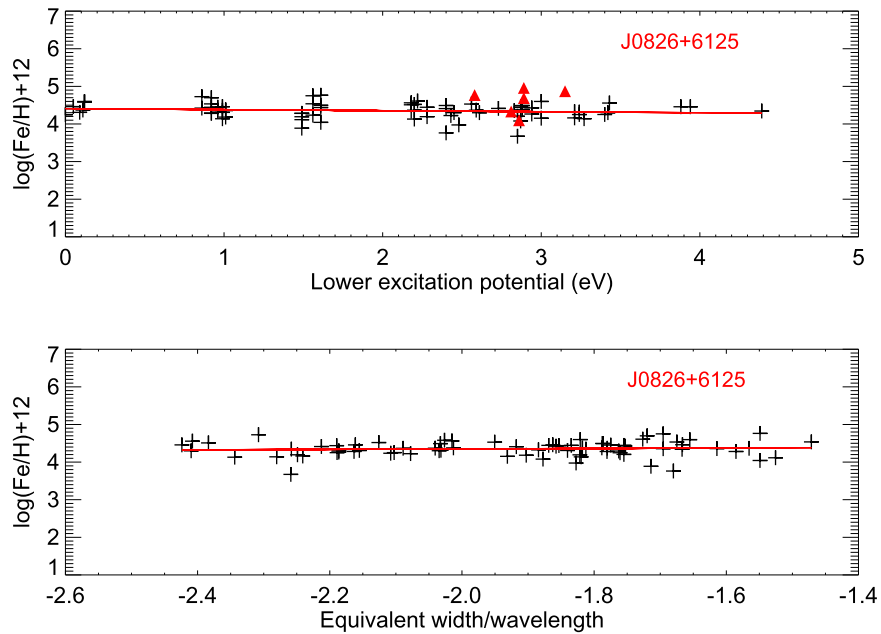
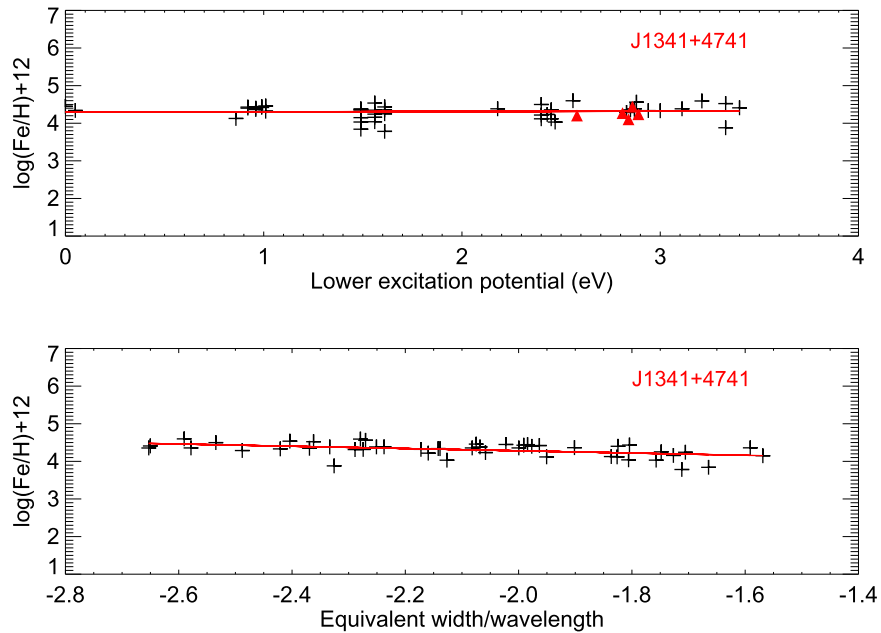


Figure 5. Top panel: Fe abundances derived from all lines, as a function of the lower excitation potential, for the adopted model for SDSS J0826+6125. Lower panel: Fe abundances, as a function of reduced equivalent widths, for the measured lines.



**Figure 6.** Top panel: Fe abundances derived from all lines, as a function of the lower excitation potential, for the adopted model for SDSS J1341+4741. Lower panel: Fe abundances, as a function of reduced equivalent widths, for the measured lines.

**Table 3**  
Estimates of Effective Temperature

Method	$T_{\text{eff}}$ (K)	
	SDSS J0826+6125	SDSS J1341+4741
$V - K$	4453	5827
SED	4500	5500
H $\alpha$	4400	5450
Fe I/Fe II	4300	5400

## 5. Abundances

### 5.1. Carbon, Nitrogen, and Oxygen

Carbon-abundance estimates for our stars were derived by iteratively fitting the CH bandhead region with synthetic spectra, and adopting the value that yields the best match. We used the CH molecular line list compiled by Bertrand Plez (Plez & Cohen 2005). The CN and CH molecular linelists were taken from the Kurucz database.

For SDSS J0826+6125, the O I line at 630 nm was used to measure the oxygen abundance, which was found to be strongly enhanced,  $[\text{O}/\text{Fe}] = +0.91$ . The chemical equilibrium of CO is taken into consideration in the turbospectrum synthesis code (de Laverny et al. 2012). We also had CO spectra and, though noisy, their oxygen abundance was consistent with the estimates from O I. The carbon abundance was obtained from the CH  $G$ -band region, which yielded a value of  $[\text{C}/\text{Fe}] = -0.82$ . We also checked the sensitivity of the CH band for various O abundances, but no variation could be detected. The  $\text{C}_2$  molecular band at 516.5 nm also could not be detected, which is consistent with a low C abundance. We could also detect the bandhead in the region of the CN band at 3884 Å, and obtain an enhancement in nitrogen corresponding to a value of  $[\text{N}/\text{Fe}] = +1.27$ .

For SDSS J1341+4741, the derived fit to the CH  $G$ -band yielded  $[\text{C}/\text{Fe}] = +0.99$ , clear evidence for its enhancement. Using medium-resolution spectroscopy from SDSS, Fernández-Alvar et al. (2016) had previously reported a carbon abundance

ratio of  $[\text{C}/\text{Fe}] = +0.95$ . The O I line at 630 nm is too weak to be detected, hence no meaningful O abundance could be derived for this star. The S/N at the region of CN band is too low to confirm enhancement in nitrogen for this star; so we could only obtain an upper limit of  $[\text{N}/\text{Fe}] < +2.37$ .

Fits for in the region of the CH  $G$ -band are shown for both stars in Figure 8.

### 5.2. The $\alpha$ -elements

Several magnesium lines were detected in the spectra of our target stars. Two of the lines in the  $\text{Mg}_g$  triplet at 5172 Å, and three other lines at 4167, 4702, and 5528 Å, were used to obtain the abundances. The derived  $[\text{Mg}/\text{Fe}]$  ratios for SDSS J0826+6125 and SDSS J1341+4741 are  $[\text{Mg}/\text{Fe}] = +0.56$  and  $[\text{Mg}/\text{Fe}] = +0.71$ , respectively, values often found among halo stars. The silicon lines at 5268 and 6237 Å were too weak to be used for abundance estimates of SDSS J0826+6125, but for SDSS J1341+4741, we obtained  $[\text{Si}/\text{Fe}] = +1.0$ . It should be noted that Si may appear over-abundant for metal-poor stars because LTE results are known to overestimate the true value (Shi et al. 2012).

Eight and 11 Ca I lines were detected in the spectra of SDSS J0826+6125 and SDSS J1341+4741, respectively, including the prominent lines at 4226.73, 4302.53, and 4454.78 Å, and used to measure its abundance. The measurements indicated slightly enhanced ratios of  $[\text{Ca}/\text{Fe}] = +0.46$  (for SDSS J0826+6125) and  $[\text{Ca}/\text{Fe}] = +0.48$  (for SDSS J1341+4741). The overall abundance of the  $\alpha$ -elements was consistent with the typical halo enhancement of  $[\alpha/\text{Fe}] = +0.4$ .

The complete list of abundances for all the elements measured in SDSS J0826+6125 and SDSS J1341+4741 are given in Tables 5 and 6 respectively. The linelists for these two stars are documented in the appendix in Tables 7 and 8.

### 5.3. The Odd-Z Elements

The sodium abundance was determined from the Na  $D_1$  and  $D_2$  resonance lines at 5890 and 5896 Å. The aluminium abundance was obtained from one of the resonance lines at

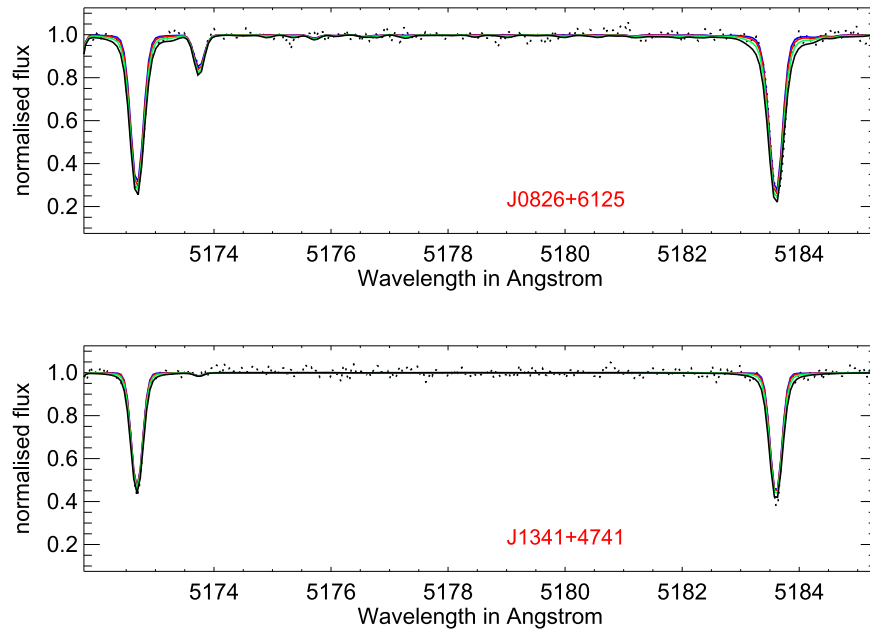


**Figure 7.** High-resolution HESP spectra of SDSS J0826+6125 (upper panel) and SDSS J1341+4741 (lower panel) in the region of the Mg I triplet for different values of  $\log(g)$ , in steps of 0.25 dex. The red solid line indicates the best-fit synthetic spectrum. The adopted parameters for SDSS J0826+6125 are  $T_{\text{eff}} = 4300$  K and  $\log(g) = 0.40$ , while those for SDSS J1341+4741 are  $T_{\text{eff}} = 5450$  K and  $\log(g) = 2.50$ .

**Table 4**  
Adopted Stellar Parameters

Object	$T_{\text{eff}}$ (K)	$\log(g)$	$\xi$	[Fe/H]
SDSS J0826+6125	4300	0.40	1.80	-3.10
SDSS J1341+4741	5450	2.50	1.80	-3.20

**Table 5**  
Elemental Abundance Determinations for SDSS J0826+6125

Elements	Species	$N_{\text{lines}}$	$A(X)$	Solar	[X/H]	[X/Fe]	$\sigma^*$
C <sup>s</sup>	CH	...	4.60	8.43	-3.92	-0.82	0.04
N <sup>s</sup>	CN	...	6.00	7.83	-1.83	+1.27	0.03
O <sup>s</sup>	O I	...	6.50	8.69	-2.19	+0.91	0.01
Na <sup>s</sup>	Na I	2	3.30	6.21	-2.91	+0.19 <sup>b</sup>	0.01
Mg <sup>s</sup>	Mg I	4	5.05	7.59	-2.54	+0.56	0.01
Al <sup>s</sup>	Al I	1	3.40	6.43	-3.03	+0.07 <sup>b</sup>	0.02
Ca	Ca I	8	3.68	6.32	-2.64	+0.46	0.06
Sc <sup>s</sup>	Sc II	5	-0.06	3.15	-3.21	-0.11	0.01
Ti	Ti I	7	1.96	4.93	-2.97	+0.13	0.03
	Ti II	6	2.06	4.93	-2.87	+0.23	0.04
Cr	Cr I	3	2.10	5.62	-3.52	-0.42	0.05
	Cr II	2	2.35	5.62	-3.27	-0.17	0.05
Mn <sup>s</sup>	Mn I	4	1.60	5.42	-3.82	-0.72	0.02
Co <sup>s</sup>	Co I	2	2.00	4.93	-2.93	+0.17	0.01
Ni	Ni I	3	3.00	6.20	-3.20	-0.10	0.04
Zn	Zn I	2	1.50	4.56	-2.96	+0.14	0.05
Sr <sup>s</sup>	Sr II	2	-0.90	2.83	-3.73	-0.63	0.01
Y <sup>s</sup>	Y II	1	-1.47	2.21	-3.68	-0.58	0.01
Zr <sup>s</sup>	Zr II	2	-0.75	2.59	-3.34	-0.24	0.01
Ba <sup>s</sup>	Ba II	2	-1.80	2.25	-4.05	-0.95	0.01

**Notes.**  $\sigma^*$  indicates the error.

<sup>b</sup> Values obtained after applying non-local thermodynamic equilibrium corrections.

<sup>s</sup> Indicates abundances obtained using synthesis.

3961.5 Å. This line is not the ideal indicator, as it can have large departures from LTE, as discussed by Baumüller & Gehren (1997), who found it to be as large as +0.6 dex.

**Table 6**  
Elemental Abundance Determinations for SDSS J1341+4741

Elements	Species	$N_{\text{lines}}$	$A(X)$	Solar	[X/H]	[X/Fe]	$\sigma^*$
Li <sup>s</sup>	Li I	1	1.95	...	...	...	0.01
C <sup>s</sup>	CH	...	6.22	8.43	-2.21	+0.99	0.04
N <sup>s</sup> †	CN	...	7.00	7.83	-0.83	+2.37	0.05
Na <sup>s</sup>	Na I	2	2.80	6.21	-3.41	-0.21 <sup>b</sup>	0.01
Mg <sup>s</sup>	Mg I	5	5.10	7.59	-2.49	+0.71	0.01
Al <sup>s</sup>	Al I	1	3.2	6.43	-3.23	-0.03 <sup>b</sup>	0.02
Si	Si I	1	5.33	7.51	-2.18	+1.02	0.07
Ca	Ca I	11	3.60	6.32	-2.72	+0.48	0.05
Sc <sup>s</sup>	Sc II	3	-0.1	3.16	-3.26	-0.06	0.01
Ti	Ti I	4	2.23	4.93	-2.70	+0.50	0.05
	Ti II	13	1.89	4.93	-3.04	+0.16	0.04
Cr	Cr I	6	2.31	5.62	-3.31	-0.11	0.04
	Cr II	1	2.77	5.62	-2.85	+0.35	0.06
Mn	Mn I	5	1.89	5.42	-3.53	-0.33	0.05
Co	Co I	2	1.99	4.93	-2.96	+0.24	0.05
Ni	Ni I	4	3.35	6.20	-2.85	+0.35	0.04
Sr <sup>s</sup>	Sr II	2	-0.88	2.83	-3.71	-0.51	0.01
Ba <sup>s</sup>	Ba II	2	-1.68	2.25	-3.93	-0.73	0.01

**Notes.** † Only upper limits could be derived.  $\sigma^*$  indicates the error.

<sup>b</sup> Values obtained after applying non-local thermodynamic equilibrium corrections.

<sup>s</sup> Indicates abundances obtained using synthesis.

Gratton et al. (2001) showed that incorporation of these corrections improves the agreement between the values of aluminum abundances obtained from this line and the high-excitation infrared doublet at 8773 Å, in the case of globular cluster dwarfs. Hence, we applied this non-LTE correction to Al in our abundance table. Aluminum is slightly enhanced for SDSS J0826+6125, while Na tracks the iron content of the stars. The scandium content is also very similar to iron. Na and Al are produced by the Ne–Na and Mg–Al cycles in intermediate and massive stars during H-shell burning. Sodium and aluminum in the two stars could be due to a well-mixed

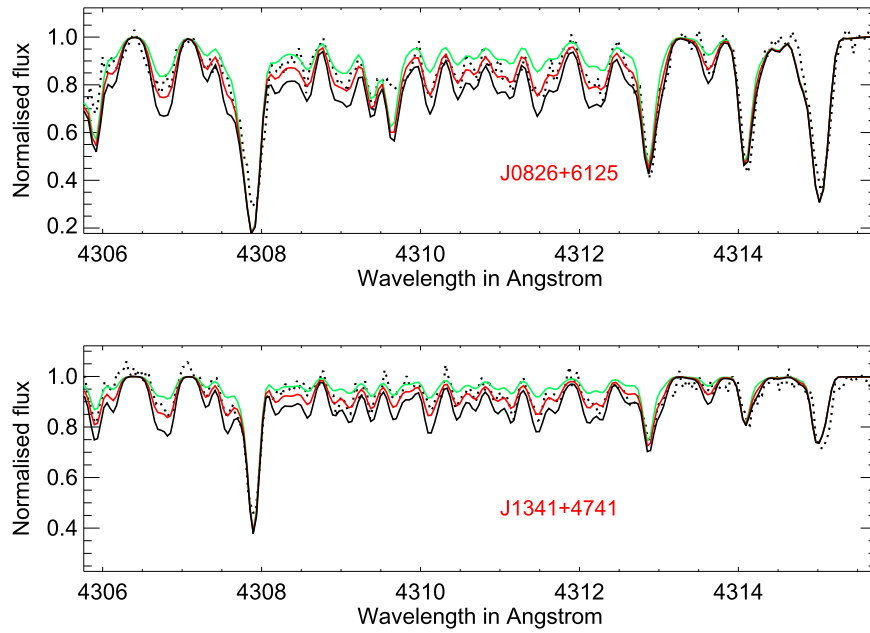


**Figure 8.** High-resolution HESP spectra in the CH G-band region for SDSS J0826+6125 (upper panel) and SDSS J1341+4741 (lower panel). The red solid line indicates the synthetic spectrum corresponding to the best fit, overplotted with two synthetic spectra with carbon 0.20 dex higher and lower than the adopted value.

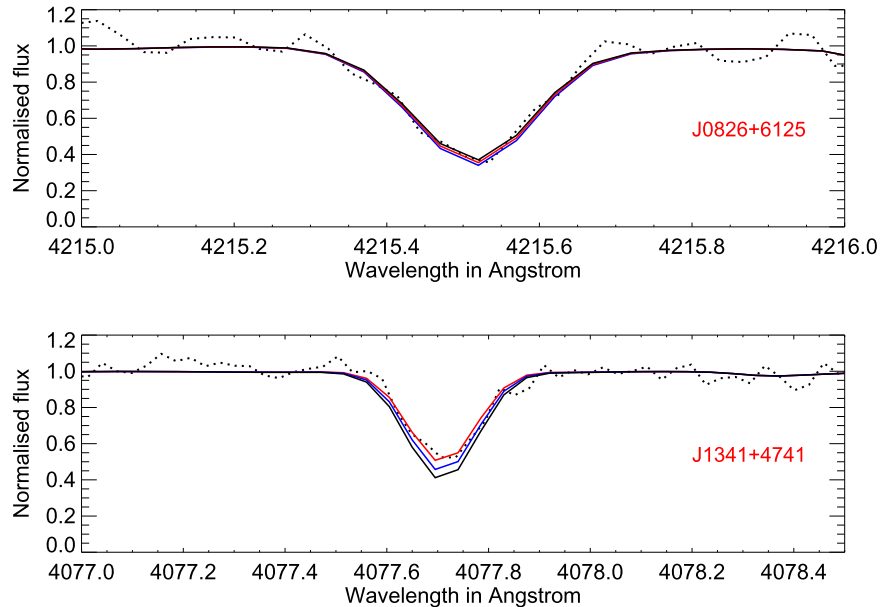


**Figure 9.** Synthesis in the Sr II region for SDSS J0826+6125 (upper panel) and SDSS J1341+4741 (lower panel). The red line indicates the best fit, overplotted with two synthetic spectra with Sr abundance 0.20 dex higher and lower than the adopted value.

interstellar medium, and are unlikely to have received direct contribution from intermediate-mass or massive-star winds.

#### 5.4. The Iron-peak Elements

Iron abundances for SDSS J0826+6125 were calculated using 82 Fe I lines and 7 Fe II lines found in the spectra; a difference of 0.3 dex was noted between the derived abundances. This difference between Fe I and Fe II is in agreement with the non-local thermodynamic equilibrium (NLTE) effects explored by Asplund (2005). Iron abundances for SDSS J1341+4741 were calculated using the 49 Fe I lines and seven Fe II lines found in the spectra; a difference

of 0.5 dex between the abundance values obtained from these lines was found, which is rather large.

We also detected the iron-peak elements Mn, Cr, Co, Ni, and Zn in our target stars. Mn and Cr are products of incomplete explosive silicon burning, and their abundances decrease with decreasing metallicity (McWilliam et al. 1995; Ryan et al. 1996; Carretta et al. 2002). For SDSS J0826+6125, the abundance of Mn was derived from the resonance Mn triplet at 4030 Å and three weaker lines near 4780 Å. Cr abundance was measured from four lines, including the stronger ones at 4646 Å and 5206 Å. Products of complete silicon burning, such as Co, Ni, and Zn, were also found in this star; all of these elements were found to track the iron content. For SDSS J1341

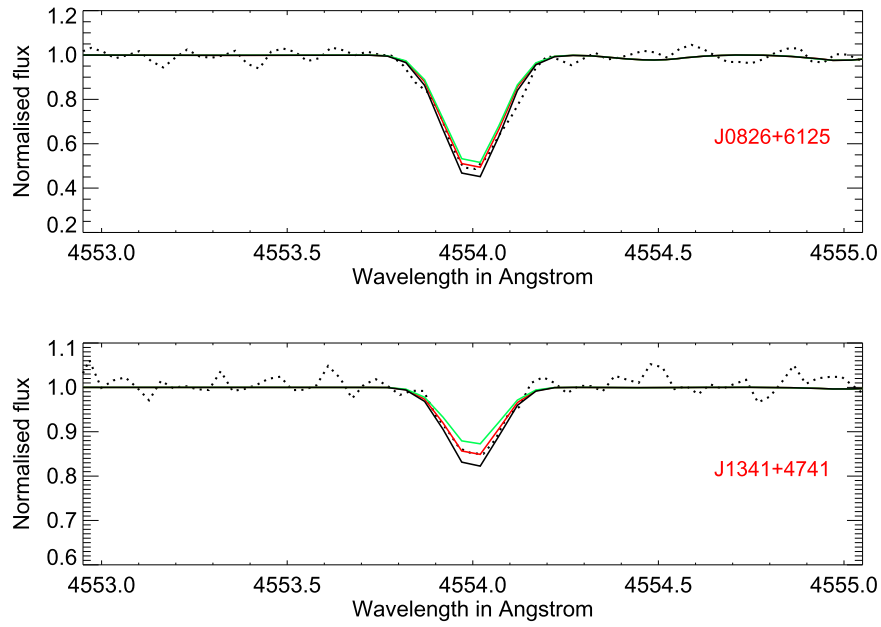


**Figure 10.** Synthesis in the Ba II region for SDSS J0826+6125 (upper panel) and SDSS J1341+4741 (lower panel). The red line indicates the best fit, overplotted with two synthetic spectra with Ba abundance 0.20 dex higher and lower than the adopted value.

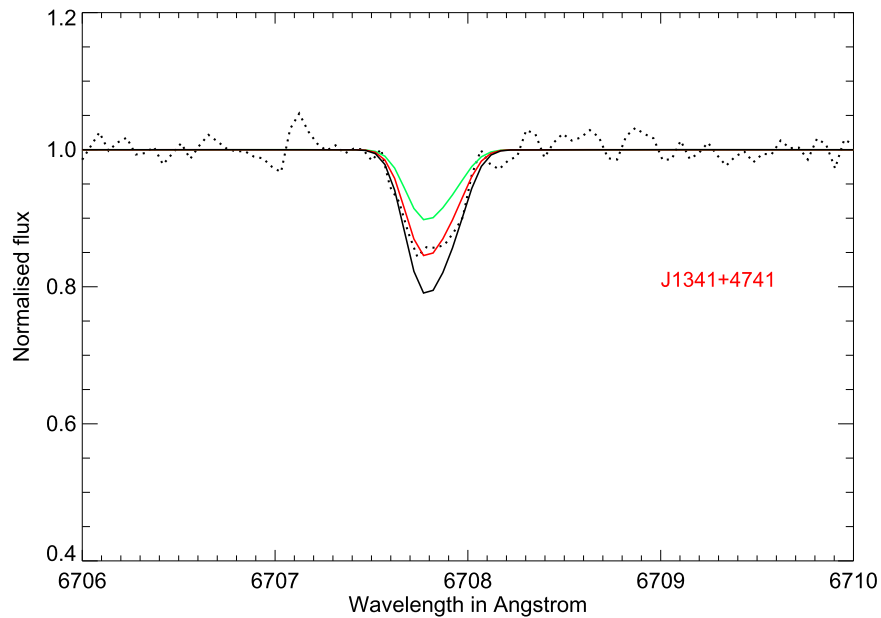


**Figure 11.** Synthesis of lithium for SDSS J1341+4741 at 6707 Å. The red line indicates the best fit, overplotted with two synthetic spectra with Li abundance 0.20 dex higher and lower than the adopted value of  $A(\text{Li}) = 1.95$ .

+4741, the abundance of Mn was derived from the resonance Mn triplet at 4030 Å and an additional line at 3823 Å. The observed abundances of Mn and Cr were similar to other EMP stars. The abundance derived for Ni using the four lines of this element present in the spectrum of SDSS J1341+4741 is clearly higher relative to iron,  $[\text{Ni}/\text{Fe}] = +0.35$ .

### 5.5. The Neutron-capture Elements

Strontium and barium are the two neutron-capture elements detected in the spectra of SDSS J1341+4741. Resonance lines of Sr II at 4077 and 4215 Å were detected in both of our target stars. SDSS J0826+6125 was found to be under-abundant

in both strontium and barium, with abundances of  $[\text{Sr}/\text{Fe}] = -0.63$  and  $[\text{Ba}/\text{Fe}] = -0.95$ , respectively. The other neutron-capture elements found in this star were Y and Zr, which were under-abundant as well. SDSS J1341+4741 was also found to be under-abundant in strontium compared to the solar ratio,  $[\text{Sr}/\text{Fe}] = -0.51$ . Ba II resonance lines at 4554 and 4937 Å were also measured, and exhibited a considerable barium depletion,  $[\text{Ba}/\text{Fe}] = -0.73$ . Based on the clear under-abundance of the neutron-capture elements, along with its strong carbon over-abundance, this star can be confidently classified as a CEMP-no star.

Best-fit spectra of the Sr and Ba syntheses for our two stars are shown in Figures 9 and 10.



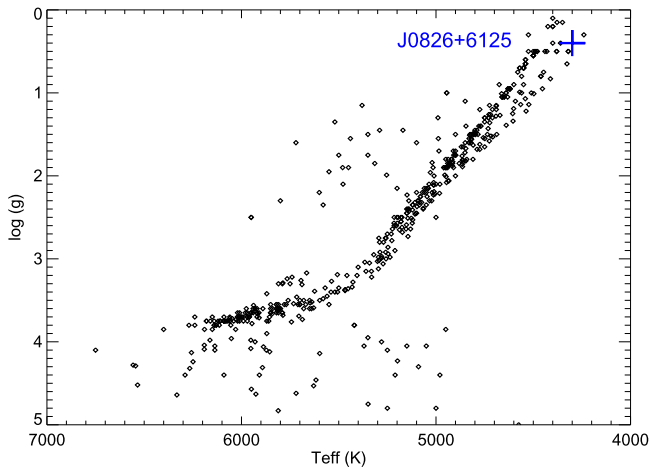


**Figure 12.** Position of SDSS J0826+6125 among other EMP halo stars in the  $\log(g)$ – $T_{\text{eff}}$  plane. The position of the star at the tip of the RGB is marked by the blue cross.

### 5.6. Lithium

Although lithium was not detected in SDSS J0826+6125, there is a strong feature observed in SDSS J1341+4741 at 6707 Å, the Li doublet, from which we obtain an abundance  $A(\text{Li}) = 1.95$ , which is similar to some other CEMP-no stars (e.g., Sivarani et al. 2006, Matsuno et al. 2017). The detection of lithium indicates that this star is unlikely to have experienced AGB binary mass transfer or direct winds from a massive star. Mass transfer from a low-mass AGB would produce large amounts of carbon and deplete lithium, along with the production of  $s$ -process-enhanced material. A ( $4\text{--}7 M_{\odot}$ ) AGB star that had experienced hot bottom burning would produce abundant nitrogen and very low carbon. There are some models in which AGB stars could produce lithium through the Cameron–Fowler mechanism (Cameron & Fowler 1971). It is unclear if an AGB with mass  $3\text{--}4 M_{\odot}$  could explain the observed C, N, low  $s$ -process elements, and lithium. Evolutionary mixing inside the star in its subgiant phase might deplete the original lithium abundance of the star-forming cloud. The synthesis for this element is shown in Figure 11.

## 6. Discussion

### 6.1. SDSS J082625.70+612515.10

#### 6.1.1. Carbon, Nitrogen, and the Non-detection of Lithium

In the *First Stars VI* paper, Spite et al. (2005) found that carbon and nitrogen were anti-correlated, and the faint halo stars could be classified into two groups: “unmixed” stars, which exhibited C enhancement with N depletion, having  $A(\text{Li})$  between 0.2 and 1.2, and “mixed” stars, which showed  $[\text{C}/\text{Fe}] < 0.0$ ,  $[\text{N}/\text{Fe}] > +0.5$ , and Li below the detection threshold. SDSS J0826+6125 clearly falls into the second group. Lithium is a very fragile element, which is destroyed at temperatures in excess of 2.5 million K. Evidence for this can be seen in previous samples of metal-poor stars; the  $A(\text{Li}) = 2.3$  observed for metal-poor dwarfs starts decreasing as the star ascends the giant branch, to  $A(\text{Li}) < 1.2$  for giants (*First Stars VII*; Bonifacio et al. 2007). The non-detection of lithium for this star could be understood in this way.

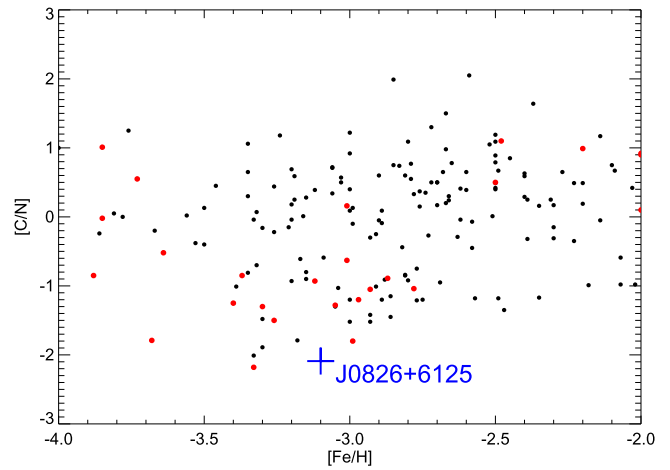


**Figure 13.** Very low  $[\text{C}/\text{N}]$  abundance ratio compared to other low-metallicity C-poor halo stars. SDSS J0826+6125 is marked by the blue cross. The red dots mark the stars at the tip of the RGB with  $\log(g) < 1$ .

In *First Stars IX*, Spite et al. (2006) argued that such destruction could be taken as a signature of mixing, and placed this mixed group of stars higher up in the giant-branch stage of evolution. Other scenarios for depletion of lithium, such as binary mass transfer, can be eliminated for SDSS J0826+6125, as no such peculiar chemical imprints have been found. During mixing, material from deeper layers, where carbon is converted to nitrogen, is brought to the stellar surface. Figure 4 of Cayrel et al. (2004) shows the decline in the value of  $[\text{C}/\text{Fe}]$  for temperatures below 4800 K in metal-poor stars, which is again attributed to deep mixing at lower temperatures. With a  $T_{\text{eff}}$  of 4300 K and a low  $\log(g) = 0.4$ , SDSS J0826+6125 can be placed in the mixed group of stars close to the tip of the red giant branch (RGB). Figure 12 shows the position of the star in the  $\log(g)$ – $T_{\text{eff}}$  plane, compared with other metal-poor halo stars compiled in the SAGA database (Suda et al. 2008). It sits right at the tip of the RGB. Figure 13 compares the  $[\text{C}/\text{N}]$  ratio with the metallicity of the halo stars having carbon deficiency (and for which both estimates of carbon and nitrogen are available). The abundance ratio of  $[\text{C}/\text{N}]$  for SDSS J0826+6125 is remarkably low compared to other stars at the tip of the RGB.

#### 6.1.2. The Light Elements

SDSS J0826+6125 exhibits a low Na, high Mg, and low Al content, consistent with the odd–even pattern expected to occur during massive-star nucleosynthesis at low metallicities. A slight enhancement of Na is observed, which could be an imprint of the previous generations of stars that underwent the Ne–Na cycle, as it is not possible to produce these elements in the RGB phase. Such an anomaly could be similar to that seen in globular cluster stars (Gratton et al. 2001, 2004), which have undergone the AGB phase and passed on processed material to a subsequent generation of star formation in a closed system. Unfortunately, other signatures seen in globular cluster stars, such as the C–N–O and O–Na–Mg–Al correlations and anti-correlations (Shetrone 1996; Gratton et al. 2004; Carretta et al. 2010; Coelho et al. 2011; Mészáros et al. 2015) were not observed in this star.

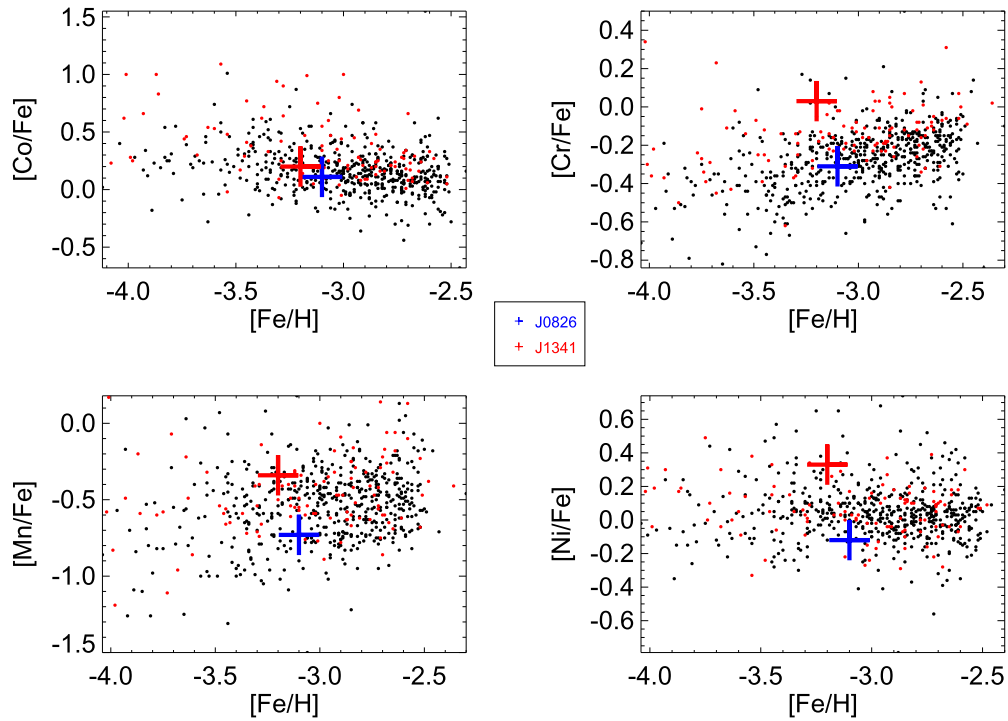


**Figure 14.** Distribution of Fe-peak elements for Galactic halo stars. The red dots represent the CEMP-no stars, while black dots represent C-normal halo stars. The two program stars SDSS J0826+6125 and SDSS J1341+4741 are indicated by blue and red crosses, respectively.

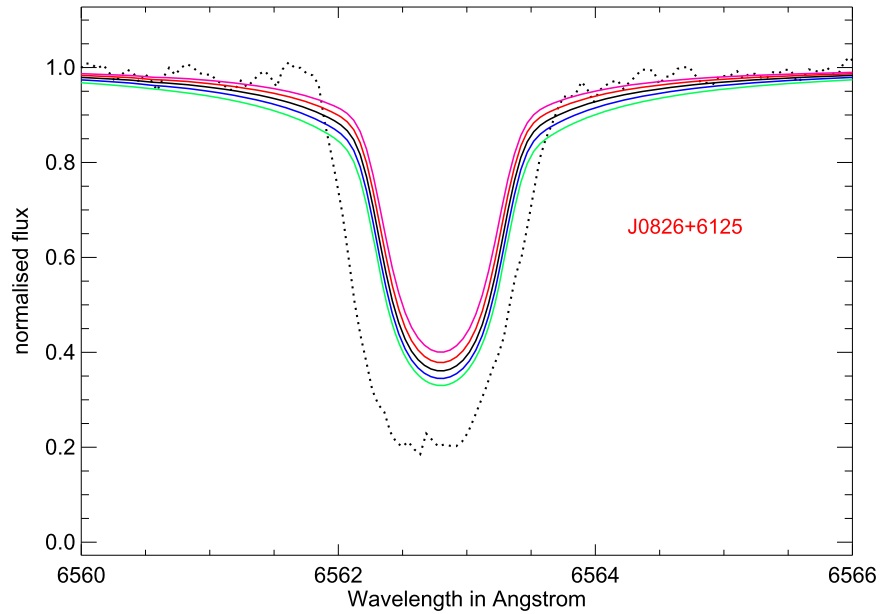


**Figure 15.** Strange  $H_{\alpha}$  profile of SDSS J0826+6125, for different values of temperature from 4200 to 4600 K in steps of 100 K.

### 6.1.3. The Iron-peak Elements

Abundances of Fe-peak elements (Cr, Mn, Co, and Ni) for metal-poor stars from the SAGA database are plotted, as a function of metallicity, in Figure 14, along with the position of SDSS J0826+6125. This star appears to be relatively rich in Co, but poor in Cr, Mn, and Ni, consistent with McWilliam et al. (1995) and Audouze & Silk (1995), who showed the same trends for several stars with metallicity below  $[\text{Fe}/\text{H}] = -2.4$ . The relative abundances of the Fe-peak nuclei can be well

explained by their dependence on the mass cut of the progenitor supernova with temperature, which gives rise to a photo-disintegration process (Woosley & Weaver 1986).

### 6.1.4. The Neutron-capture Elements

Abundances of both the heavy and light  $s$ -process elements found in SDSS J0826+6125 are low, which is again consistent with the lack of available neutron flux (Audouze & Silk 1995). The abundance values are very similar to other EMP giants.

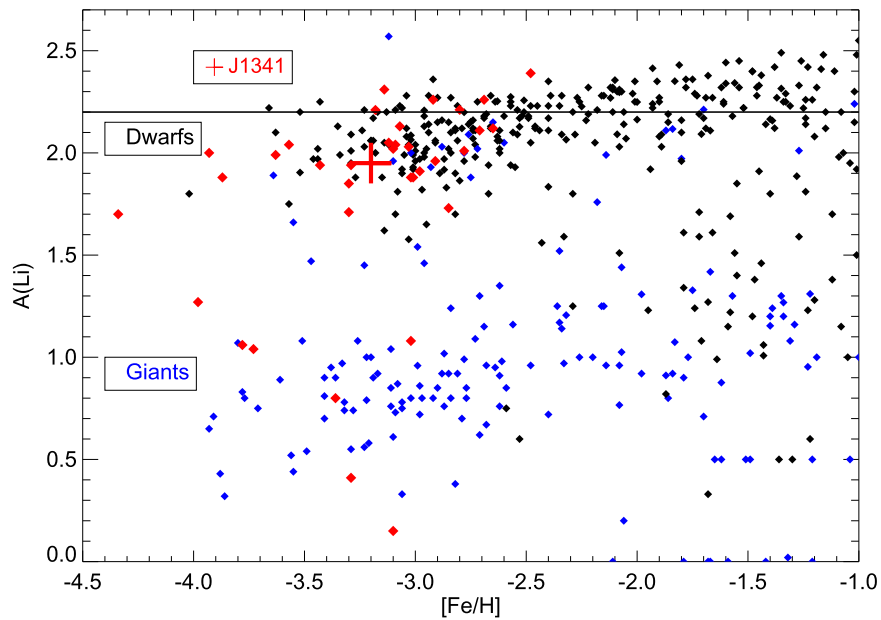


**Figure 16.** Comparison of the observed lithium for CEMP-no stars, taken from the SAGA database. The blue dots mark the EMP giants while black dots are the EMP dwarfs. Red points are the CEMP-no stars. The red cross marks the location of SDSS J1341+4741.

### 6.1.5. The Asymmetric $H_{\alpha}$ Profile of J0826+6125

SDSS J0826+6125 was observed several times, and an asymmetry in the  $H_{\alpha}$  profile was noted for all of the spectra. The profile also could not be well-fit with synthetic spectra. The  $H_{\alpha}$  profile and its fit with the model spectrum is shown in Figure 15. This could be due to the inadequacy of the 1D stellar models, or it may be due to an extended atmosphere present in the star. The  $H_{\alpha}$  profile was also found not to be varying over several observation epochs, indicating no ongoing mass transfer. The extended atmosphere could be the result of past mass transfer from an intermediate-mass AGB companion, or mixing due to first dredge-up of the star in the RGB phase. It is also possible that the star itself is an AGB star (e.g., Masseron et al. 2006).

## 6.2. SDSS J134144.60+474128.90

### 6.2.1. Lithium

We obtained a measurement of  $A(\text{Li}) = 1.95$  for SDSS J1341+4741, which is lower than the Spite Plateau (Spite & Spite 1982) value of  $A(\text{Li}) = 2.2 \pm 0.1$  (Pinsonneault et al. 1999), and much lower than the predicted amount of Li from big bang nucleosynthesis ( $A(\text{Li}) = 2.75$ ; Steigman 2005). Our limited RV information for this star indicates a clear variation, from which we derive a possible period of 116 days. However, we have no other evidence that a mass-transfer event may have occurred. The distribution of lithium for CEMP-no stars, along with other EMP stars, is shown in Figure 16. According to the analysis of Meynet et al. (2010) and Masseron et al. (2012), this star falls close to the edge of Li-depleted stars ( $A(\text{Li}) = 2.00$  is adopted as the separation between Li-normal and Li-depleted metal-poor stars). A slight depletion from the Spite Plateau value could be attributed to internal mixing of the star, or the observed value of lithium for SDSS J1341+4741 may be the result of several concurrent phenomena.

1. The ejected material from the progenitor SN will have depleted Li abundance along with other nucleosynthetic elements and enhanced carbon (for the case of SDSS J1341+4741) that is mixed with the primordial cloud. Depending upon the dilution factor in the natal cloud, it may be possible to achieve the necessary Li value (Piau et al. 2006; Meynet et al. 2010; Maeder et al. 2015).
2. A Spite Plateau value of Li was present in the natal cloud of SDSS J1341+4741, and it is depleted by thermohaline mixing or meridional circulation (Masseron et al. 2012) in the star. If we consider the current evolutionary state of the star to be in the RGB phase, this could be a viable mechanism.
3. Enhanced rotationally induced mixing in the RGB phase (following Denissenkov & Herwig 2004) can lead to formation of lithium in the star, following depletion of all the primordial Li. It is very difficult to differentiate between an AGB or a massive rotating star as the precursor using Li as the sole yardstick, as both result in almost the same nucleosynthetic yield of Li (Meynet et al. 2006; Masseron et al. 2012).

### 6.2.2. Carbon

According to Spite et al. (2013) and Bonifacio et al. (2015), CEMP stars are distributed along two bands in the  $A(\text{C})$  versus  $[\text{Fe}/\text{H}]$  plane. The upper band is centered around  $A(\text{C}) \sim 8.25$ , and comprises relatively more metal-rich CEMP-*s* stars, while the lower band centered around  $A(\text{C}) \sim 6.50$  comprises more metal-poor, and primarily CEMP-no, stars. Further investigation by Hansen et al. (2016b) also led to the result that the majority of the stars that are known binaries lie close to the upper band.

By expanding the list of CEMP stars with available high-resolution spectroscopic analyses to include more evolved subgiants and giants (with the later giants having C abundances

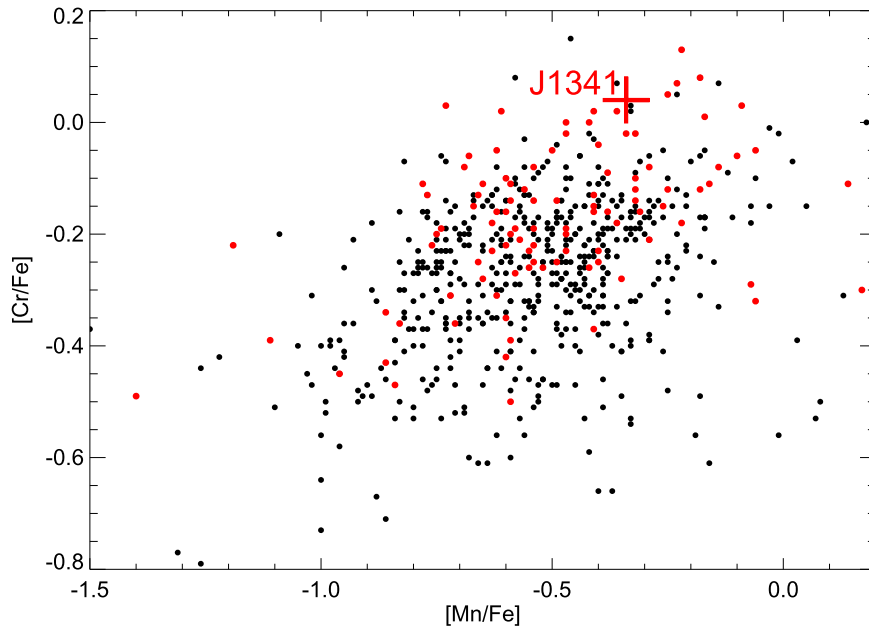


**Figure 17.** Relative enhancement of Cr and Mn for SDSS J1341+4741, shown as a red cross, in the  $[\text{Cr}/\text{Fe}]$  vs.  $[\text{Mn}/\text{Fe}]$  space. Red dots mark the CEMP-no stars while the black dots mark the EMP stars.

corrected for evolutionary mixing effects; Placco et al. 2014), Yoon et al. (2016) demonstrated that the morphology of this abundance space is more complex, with three prominent groups identified in the so-called Yoon–Beers diagram (their Figure 1). They argued that a separation between CEMP-*s* stars and CEMP-no stars in their sample could be reasonably achieved by splitting the sample at  $A(\text{C}) = 7.1$ , with the Group I CEMP-*s* stars lying above this level and the Group II and III CEMP-no stars lying below it. In this classification scheme, SDSS J1341+4741, with  $A(\text{C}) \sim 6.22$ , can be comfortably identified as a Group II CEMP-no star. Hence, the enhancement of carbon in this star is most likely to be intrinsic to it (i.e., the C was present in its natal gas), and not the result of mass transfer from an extinct AGB companion. Thus, the elemental-abundance pattern observed from this star is associated with nucleosynthesis from a core collapse SN at early times, perhaps with additional contributions from stars that formed and evolved within its natal gas cloud.

### 6.2.3. The Light Elements

SDSS J1341+4741 exhibits the low  $[\text{Na}/\text{Fe}]$ , high  $[\text{Mg}/\text{Fe}]$ , and low  $[\text{Al}/\text{Fe}]$  ratios expected from the odd–even pattern in massive-star nucleosynthesis yields at low metallicities (e.g., Arnett 1971; Truran & Arnett 1971; Peterson 1976; Umeda et al. 2000; Heger & Woosley 2002). The light elements closely follow the overall halo population observed in the Galaxy as well (Cayrel et al. 2004). Following Yoon et al. (2016), SDSS J1341+4741 is clearly a member of the Group II stars, and supports a possible mixing and fallback SN as a likely progenitor.

### 6.2.4. The Iron-peak Elements

Abundances of Fe-peak elements for SDSS J1341+4741 (Cr, Mn, Co, and Ni) are shown in Figure 14, as a function of  $[\text{Fe}/\text{H}]$ , compared with other CEMP-no and C-normal EMP stars compiled from the SAGA database (Suda et al. 2008). One feature that clearly stands out is the over-abundance of Cr

and Ni, and to some extent Mn. In the low-metallicity regime, the stars are expected to show signatures of Type II SNe nucleosynthesis. All three elements play key roles in determining the progenitor population in the halo and the subsequent SNe yields. A decrease in  $[\text{Cr}/\text{Fe}]$  and  $[\text{Mn}/\text{Fe}]$  with decreasing  $[\text{Fe}/\text{H}]$  should be accompanied with enhancement in  $[\text{Co}/\text{Fe}]$ , as a result of deeper mass cuts in the progenitor SNe (refer to Figure 9 of Nakamura et al. 1999). However, enhancement in both  $[\text{Cr}/\text{Fe}]$  and  $[\text{Mn}/\text{Fe}]$  can also be explained by an excess of neutrons. Since neutron excess is a function of metallicity, we have plotted  $[\text{Cr}/\text{Fe}]$  versus  $[\text{Mn}/\text{Fe}]$  in Figure 17 to eliminate the trend with Fe abundance (following, e.g., Carretta et al. 2002). In this plot, our program star occupies a relatively higher position amidst the population of CEMP-no stars. From Heger & Woosley (2002, 2010) and Qian & Wasserburg (2002), it is known that very massive stars ( $80 < M/M_{\odot} < 240$ ) belonging to Population III explode as pair-instability SNe, which should not produce a correlation between  $[\text{Cr}/\text{Fe}]$  and  $[\text{Mn}/\text{Fe}]$ . Thus, the presence of this correlation points us toward Type II SNe associated with a relatively high-mass ( $M/M_{\odot} < 80$ ) but not extremely high-mass progenitor.

Nickel is an extremely important element for gaining further insight into the nature of the progenitor of SDSS J1341+4741. The depth of the gravitational potential and amount of neutrino-absorbing material in the models are the two factors that compete for the production of Ni in Type II SNe. In very massive ( $M/M_{\odot} > 30$ ) stars the deeper gravitational potential restricts nickel from being ejected due to fallback, while intermediate-mass ( $10 < M/M_{\odot} < 20$ ) stars eject large amounts of Ni because of a large neutrino-absorbing region (Nakamura et al. 1999). Thus, enhancement of nickel also points in the same direction, that the progenitor is likely to be a massive ( $20 < M/M_{\odot} < 30$ ) star exploding as a Type II SN in the early Galaxy. The observations support the hypothesis of a mixing and fallback model (Nomoto et al. 2013) with a lower degree of fallback, so as to eject a larger mass of  $^{56}\text{Ni}$ .

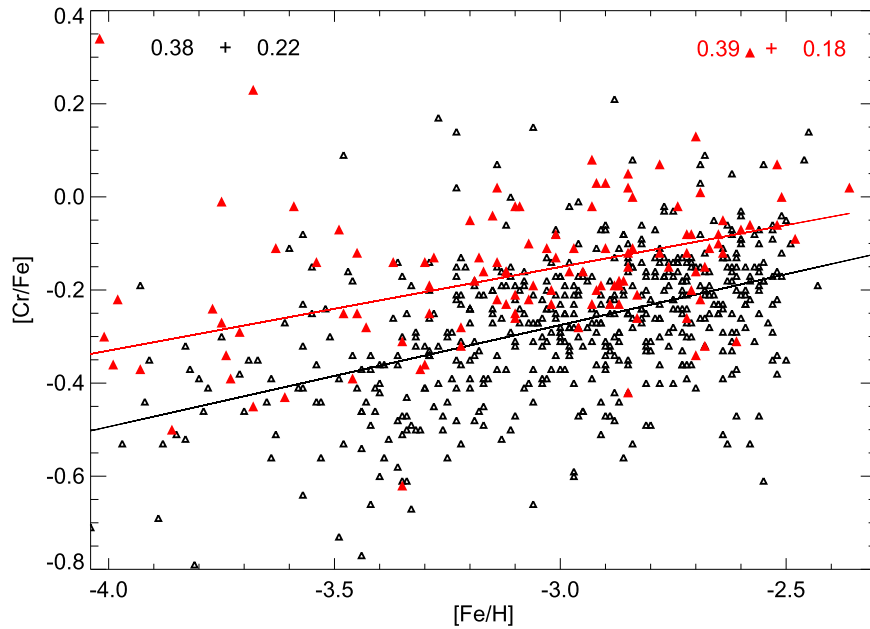


**Figure 18.** Linear fits for CEMP-no (red) and C-normal EMP stars (black). The slope and  $\sigma$  are shown for each fit in the corresponding color.

### 6.2.5. The Neutron-capture Elements

The first *s*-process peak element Sr and the second *s*-process peak element Ba have been detected in both SDSS J0826+6125 and SDSS J1341+4741, and they exhibit under-abundances. The ratio of light to heavier neutron-capture elements is sensitive to the nature of the progenitors. Neutron star mergers are expected to produce heavy neutron-capture elements (e.g., Argast et al. 2004), and have been observed to do so in the kilonova SSS17a associated with GW170817 (Kilpatrick et al. 2017), which exhibited clear evidence for the presence of unstable isotopes created by the *r*-process (Drout et al. 2017; Shappee et al. 2017). SNe with jets (e.g., Winteler et al. 2012; Nishimura et al. 2015) may also produce heavy neutron-capture elements. Formation of these systems may depend on the environment as well.

### 6.2.6. Nature of the Binary Companions of SDSS J0826+6125 and SDSS J1341+4741

Both of the program stars exhibit clear RV variations, indicating the likely presence of a binary companion. In the case of SDSS J0826+6125, the enhanced abundances of N and under-abundance of C indicate possible mixing of the atmosphere with CN-cycle products. This can result from first dredge-up mixing in the star, which is currently in the RGB, following mass transfer from an intermediate-mass AGB star that might have gone through hot bottom burning (Lau et al. 2007; Suda et al. 2012). The low  $\log(g)$  value of the star supports RGB mixing, although AGB mass transfer cannot be ruled out. The non-detection of Li and peculiar  $H_{\alpha}$  profiles could indicate either internal mixing or binary mass transfer as well. In the case of an intermediate-mass AGB that goes through hot bottom burning, the temperatures are sufficiently high for the star to operate the CNO cycle. In that case, SDSS J0826+6125 may be a true nitrogen-enhanced metal-poor (see Johnson et al. 2007; Pols et al. 2009, 2012) star, which are known to exist but are relatively rare.

In the case of SDSS J1341+4741, the binary companion did not likely contribute through a mass-transfer event, since the Li abundance in the star is similar to other EMP stars, although it is lower than the Spite Plateau value. The mild depletion of Li could be due to binary-induced mixing or internal mixing of the star during its sub-giant phase. It may well be worthwhile to mount an RV-monitoring campaign for this and other Li-depleted EMP stars to test for a possible binary-star origin to the declining lithium abundance problem for stars with  $[\text{Fe}/\text{H}] < -3.0$ .

### 6.3. CEMP-no and EMP Stars

From the above discussion, and based on previous studies, it is evident that CEMP-no and C-normal EMP stars have very different origins. Even within the sub-class of CEMP-no stars, there may well be different types of progenitors. As discussed by Yoon et al. (2016), the Group II CEMP-no stars could be associated with the faint mixing and fallback SNe, whereas the Group III CEMP-no stars can be attributed to the spinstar models, with a number of exceptions for both classes (Meynet et al. 2006; Nomoto et al. 2013). See also the discussion of the progenitors for CEMP-no stars by Placco et al. (2016). Some of the CEMP-no stars lying in the low  $A(\text{C})$  region may have a binary component, but no mass transfer is supposed to have taken place (Starkenburger et al. 2014; Bonifacio et al. 2015; Yoon et al. 2016), which is further strengthened by the only “slight” depletion of Li in SDSS J1341+4741, as described in the previous section.

Iron-peak elements can provide valuable insights regarding the nucleosynthetic yields of their progenitor SNe, as these elements cannot be produced or modified during the post main-sequence evolutionary stages of the star. Figure 14 shows the distribution of some key Fe-peak elements for both CEMP-no and C-normal EMP stars. Visual inspection suggests that Cr and Co are enhanced for the CEMP-no population. We have compiled data from the SAGA database to see if there is an enhancement of Cr in CEMP-no stars. The fit is given in

Figure 18 for [Cr/Fe]. There is a slight offset between the EMP and CEMP-no stars, but they exhibit similar increasing trends of [Cr/Fe] with [Fe/H]. We have checked, and these behaviors apply to both dwarfs and giants. A similar offset can also be noted for Co.

Lai et al. (2008) and Bonifacio et al. (2009) have considered the discrepancies in the behavior of Cr between giants and dwarfs, since Cr II could be measured only in giants, while Cr I is a resonance line, and could suffer substantial NLTE effects. However, such issues are not expected to play a substantial role when we compare only giants with giants or dwarfs with dwarfs. Temperature and gravity do not play a major role in deviations from LTE abundances (Bergemann & Cescutti 2010), so we have not used them to further refine our sample from the archival data.

Enhancement in [Cr/Fe] for CEMP-no stars with respect to C-normal EMP stars can play a key role for understanding of the SNe ejecta and relevant mass cuts. It would be very interesting to investigate the origin of this discrepancy.

## 7. Conclusion

We have derived LTE abundances for SDSS J082625.70+612515.10; it is mostly consistent with behavior of other halo stars. The depletion in carbon and enhancement in nitrogen could be due to internal mixing within the star. It is unlikely that self-enrichment similar to that seen in globular clusters has occurred, due to the over-abundance in oxygen. The peculiar  $H_\alpha$  profile of SDSS J0826+6125 also supports the possibility of mixing that might occur in an extended atmosphere. The RV variation strongly suggests this star is a member of a binary system, but it is likely there is no ongoing mass transfer, due to the non-variable peculiar  $H_\alpha$  profile over a period of one year.

SDSS J134144.60+474128.90 is a CEMP-no type star, and likely to be a member of a binary system. The lithium is detected and mildly depleted, similar to other EMP stars. Lithium in EMP dwarfs and CEMP-no stars exhibits similar trends at different metallicities. Below [Fe/H] < -3.0, EMP and CEMP-no stars often have lithium abundance below the Spite Plateau. We also studied the trends of heavy elements among EMP and CEMP stars. At a given metallicity, CEMP-no stars appear to have larger abundances of Cr. This might provide important clues to the nature of the progenitors that contributed to the origin of carbon.

We would like to take this opportunity to thank the HESP team for successful installation and maintenance of the high-resolution spectroscopy at the Hanle telescope, despite the numerous challenges and hurdles that were encountered along the way. We would especially like to thank Amit Kumar, M N Anand, Sriram and Kathiravan for their efforts. We also extend our gratitude toward the observation team, namely Kiran B.S., Pramod Kumar, Lakshmi Prasad and Venkatesh Shankar for their tireless efforts.

T.C.B. acknowledges partial support from grant PHY 14-30152 (Physics Frontier Center/JINA-CEE), awarded by the U.S. National Science Foundation (NSF). T.M. acknowledges support provided by the Spanish Ministry of Economy and Competitiveness (MINECO) under grant AYA-2017-88254-P.

## Appendix

**Table 7**  
Linelist for SDSS J0826+6125

Species	$\lambda$	Obs.eqw	Error <sup>a</sup>	Abundance
Ca I	4425.437	34.000	1.806	3.284
Ca I	4435.679	27.600	1.628	3.239
Ca I	5594.462	30.300	1.705	3.574
Ca I	6122.217	61.900	2.437	3.729
Ca I	6162.173	82.000	2.805	3.867
Ca I	6439.075	53.600	2.268	3.598
Ca I	6449.808	8.000	0.876	3.870
Ti I	4981.731	54.800	2.293	1.884
Ti I	4991.065	52.700	2.249	1.970
Ti I	4999.503	40.600	1.974	1.851
Ti I	5007.210	52.100	2.236	2.188
Ti I	5014.187	49.600	2.182	2.301
Ti I	5064.653	30.200	1.702	1.804
Ti I	5210.385	43.000	2.031	1.905
Ti II	4470.857	45.400	2.087	2.107
Ti II	5129.152	39.400	1.945	2.068
Ti II	5154.070	44.900	2.076	2.275
Ti II	5185.913	28.000	1.639	1.913
Ti II	5188.680	72.500	2.638	2.054
Ti II	5381.015	36.100	1.861	2.234
Cr I	4545.945	7.700	0.860	1.986
Cr I	4646.148	44.400	2.064	2.445
Cr I	5206.038	81.300	2.793	2.170
Cr I	5298.277	10.600	1.009	1.915
Cr I	5348.312	6.700	0.802	1.849
Cr II	4558.650	8.500	0.903	2.249
Cr II	4588.199	11.400	1.046	2.574
Fe I	4147.669	68.747	2.569	4.283
Fe I	4174.913	72.100	2.631	4.513
Fe I	4175.636	23.000	1.486	3.837
Fe I	4202.029	125.300	3.468	4.195
Fe I	4206.697	90.700	2.950	4.492
Fe I	4216.220	119.900	3.392	10.028
Fe I	4233.603	63.000	2.459	3.989
Fe I	4250.787	143.600	3.712	4.707
Fe I	4260.474	89.000	2.923	3.780
Fe I	4415.123	124.700	3.460	4.140
Fe I	4442.339	73.700	2.660	4.481
Fe I	4447.717	83.500	2.831	4.900
Fe I	4489.739	99.300	3.087	4.696
Fe I	4528.614	97.500	3.059	4.521
Fe I	4602.941	69.399	2.581	4.353
Fe I	4733.592	32.500	1.766	4.349
Fe I	4736.773	27.200	1.616	4.294
Fe I	4871.318	64.599	2.490	4.216
Fe I	4872.138	68.300	2.560	4.464
Fe I	4890.755	80.000	2.771	4.539
Fe I	4891.492	85.983	2.873	4.212
Fe I	4903.310	47.600	2.137	4.394
Fe I	4918.994	82.600	2.816	4.543
Fe I	4920.502	99.200	3.086	4.563
Fe I	4939.687	68.560	2.565	4.425
Fe I	4994.130	95.200	3.023	4.709
Fe I	5001.864	34.500	1.820	4.478
Fe I	5014.943	18.900	1.347	4.499
Fe I	5049.820	73.900	2.663	4.559
Fe I	5051.635	106.799	3.202	4.689
Fe I	5068.766	33.000	1.780	4.277
Fe I	5079.740	69.700	2.586	4.504
Fe I	5083.339	89.400	2.929	4.586

**Table 7**  
(Continued)

Species	$\lambda$	Obs.eqw	Error <sup>a</sup>	Abundance
Fe I	5123.720	64.100	2.480	4.332
Fe I	5127.359	69.361	2.580	4.447
Fe I	5142.928	79.200	2.757	4.544
Fe I	5150.840	74.400	2.672	4.350
Fe I	5166.282	89.600	2.932	4.306
Fe I	5171.596	99.900	3.096	4.107
Fe I	5192.344	78.394	2.743	4.607
Fe I	5194.942	104.700	3.170	4.806
Fe I	5216.274	85.100	2.858	4.588
Fe I	5225.526	47.600	2.137	4.425
Fe I	5232.940	92.300	2.976	4.439
Fe I	5247.050	36.700	1.877	4.372
Fe I	5250.209	49.400	2.177	4.593
Fe I	5250.646	39.300	1.942	4.562
Fe I	5266.555	61.700	2.433	4.287
Fe I	5270.356	148.900	3.780	4.794
Fe I	5283.621	49.100	2.171	4.375
Fe I	5307.361	34.300	1.814	4.479
Fe I	5324.179	69.500	2.583	4.403
Fe I	5332.900	41.600	1.998	4.385
Fe I	5339.929	28.000	1.639	4.194
Fe I	5393.168	34.900	1.830	4.432
Fe I	5397.128	140.200	3.668	4.309
Fe I	5405.775	147.000	3.756	4.414
Fe I	5415.199	29.888	1.694	4.348
Fe I	5434.524	132.100	3.561	4.446
Fe I	5497.516	89.501	2.931	4.384
Fe I	5501.465	83.700	2.834	4.436
Fe I	5506.779	83.400	2.829	4.252
Fe I	5576.089	21.800	1.446	4.572
Fe I	5572.842	44.000	2.055	4.274
Fe I	5624.542	21.894	1.450	4.304
Fe I	6065.482	39.500	1.947	4.410
Fe I	6136.615	56.671	2.332	4.304
Fe I	6137.692	50.000	2.191	4.383
Fe I	6230.723	69.821	2.589	4.537
Fe I	6252.555	58.000	2.359	4.572
Fe I	6265.134	25.900	1.577	4.527
Fe I	6335.331	28.700	1.660	4.317
Fe I	6358.698	31.300	1.733	4.763
Fe I	6393.601	53.451	2.265	4.230
Fe I	6421.351	36.200	1.864	4.442
Fe I	6430.846	62.100	2.441	4.605
Fe I	6494.980	78.500	2.745	4.429
Fe I	6592.914	40.400	1.969	4.434
Fe II	4233.172	94.400	3.010	5.001
Fe II	4491.405	17.600	1.300	4.136
Fe II	4583.837	68.400	2.562	4.458
Fe II	4923.921	106.100	3.191	4.993
Fe II	5018.440	103.600	3.153	4.776
Fe II	5197.568	33.800	1.801	13.002
Fe II	5316.615	77.600	2.729	4.910
Ni I	4855.406	8.100	0.882	3.040
Ni I	6643.629	11.300	1.041	2.946
Ni I	6767.768	16.200	1.247	3.165
Zn I	4722.153	11.500	1.051	1.668
Zn I	4810.528	9.300	0.945	1.434

**Note.**

<sup>a</sup> The errors are computed using Cayrel's relation (Cayrel de Strobel & Spite 1988).

**Table 8**  
Linelist for SDSS J1341+4741

Species	$\lambda$	Obs.eqw	Error <sup>a</sup>	Abundance
Si I	5268.387	4.600	0.664	5.457
Si I	6237.319	4.200	0.635	5.358
Ca I	4226.728	112.700	3.289	3.221
Ca I	4283.011	10.300	0.994	3.401
Ca I	4302.528	23.800	1.511	3.368
Ca I	4318.652	18.700	1.340	3.710
Ca I	4425.437	27.400	1.622	3.910
Ca I	4454.779	39.600	1.950	3.558
Ca I	4585.865	12.200	1.082	3.679
Ca I	5857.451	9.100	0.935	3.834
Ca I	6122.217	28.700	1.660	3.959
Ca I	6162.173	32.700	1.772	3.841
Ca I	6439.075	21.600	1.440	3.677
Ti I	4533.241	15.600	1.224	2.419
Ti I	4981.731	13.100	1.121	2.288
Ti I	4991.065	6.000	0.759	2.036
Ti I	4999.503	9.800	0.970	2.368
Ti II	4012.385	17.500	1.296	1.789
Ti II	4028.343	21.100	1.423	2.522
Ti II	4163.648	3.200	0.554	1.598
Ti II	4171.910	3.500	0.580	1.739
Ti II	4290.219	49.800	2.186	2.259
Ti II	4300.049	53.300	2.262	1.899
Ti II	4312.864	22.400	1.466	1.933
Ti II	4395.033	58.600	2.372	1.888
Ti II	4443.794	52.200	2.238	1.965
Ti II	4468.507	57.900	2.357	2.013
Ti II	4501.273	48.400	2.155	1.974
Ti II	4533.969	49.800	2.186	1.904
Ti II	4563.761	36.600	1.874	1.887
Ti II	4571.968	31.800	1.747	1.599
Cr I	4254.332	54.600	2.289	2.187
Cr I	4274.796	59.800	2.396	2.377
Cr I	4289.716	46.200	2.106	2.240
Cr I	5204.506	14.600	1.184	2.296
Cr I	5206.038	31.900	1.750	2.504
Cr I	5208.419	39.100	1.937	2.509
Cr I	4824.127	4.300	0.642	2.834
Mn I	3823.507	37.100	1.887	3.290
Mn I	4030.753	41.100	1.986	1.622
Mn I	4033.062	15.200	1.208	1.178
Mn I	4034.483	17.900	1.311	1.449
Mn I	4823.524	3.800	0.604	2.165
Fe I	4005.242	72.350	2.635	4.325
Fe I	4045.812	109.200	3.237	4.339
Fe I	4132.058	73.770	2.661	4.379
Fe I	4143.868	77.740	2.732	4.299
Fe I	4187.039	41.910	2.006	4.452
Fe I	4187.795	36.600	1.874	4.310
Fe I	4198.304	29.080	1.671	4.306
Fe I	4202.029	73.499	2.656	4.140
Fe I	4227.427	19.970	1.384	3.934
Fe I	4250.119	31.760	1.746	4.095
Fe I	4250.787	66.470	2.526	4.165
Fe I	4260.474	63.579	2.470	4.213
Fe I	4271.154	47.860	2.143	4.437
Fe I	4271.760	92.450	2.979	3.977
Fe I	4325.762	83.979	2.839	3.897
Fe I	4375.930	41.550	1.997	4.511
Fe I	4383.545	112.400	3.284	4.508
Fe I	4404.750	86.770	2.886	4.355

**Table 8**  
(Continued)

Species	$\lambda$	Obs.eqw	Error <sup>a</sup>	Abundance
Fe I	4415.122	69.280	2.579	4.522
Fe I	4427.310	31.930	1.751	4.399
Fe I	4528.614	38.710	1.927	4.440
Fe I	4531.148	21.030	1.421	4.644
Fe I	4583.721	25.720	1.571	7.103
Fe I	4871.318	28.190	1.645	4.433
Fe I	4872.138	26.150	1.584	4.603
Fe I	4891.492	40.500	1.972	4.401
Fe I	4918.994	26.150	1.584	4.360
Fe I	5006.119	16.280	1.250	4.348
Fe I	5041.756	13.310	1.130	4.420
Fe I	5171.596	26.600	1.598	4.370
Fe I	5194.942	20.500	1.403	4.603
Fe I	5216.274	11.600	1.055	4.429
Fe I	5232.940	38.020	1.910	4.387
Fe I	5266.555	19.990	1.385	4.388
Fe I	5269.537	76.789	2.715	4.240
Fe I	5324.179	27.990	1.639	4.632
Fe I	5328.039	79.800	2.767	4.483
Fe I	5328.532	22.770	1.478	4.404
Fe I	5371.490	67.410	2.544	4.445
Fe I	5397.128	55.110	2.300	4.490
Fe I	5405.775	58.820	2.376	4.487
Fe I	5429.697	57.280	2.345	4.474
Fe I	5434.524	36.540	1.873	4.386
Fe I	5446.917	56.490	2.328	4.522
Fe I	5455.609	45.910	2.099	4.532
Fe I	5572.842	12.470	1.094	4.478
Fe I	5615.644	24.400	1.530	4.603
Fe I	6230.723	16.000	1.239	4.670
Fe I	6494.980	18.970	1.349	4.552
Fe II	4233.172	30.390	1.708	4.243
Fe II	4508.288	15.630	1.225	4.494
Fe II	4515.339	5.290	0.713	4.132
Fe II	4522.634	7.240	0.834	3.890
Fe II	4555.893	2.260	0.466	3.527
Fe II	4583.837	25.720	1.571	4.294
Fe II	4923.927	48.280	2.153	4.255
Co I	4092.384	7.900	0.871	2.267
Co I	4121.311	11.400	1.046	1.823
Ni I	3807.138	30.300	1.705	2.603
Ni I	4401.538	7.000	0.820	3.374
Ni I	4459.027	22.000	1.453	4.258
Ni I	5476.900	20.600	1.406	3.348

**Note.**<sup>a</sup> The errors are computed using Cayrel's relation (Cayrel de Strobel & Spite 1988).**ORCID iDs**Avrajit Bandyopadhyay  <https://orcid.org/0000-0002-8304-5444>Antony Susmitha  <https://orcid.org/0000-0002-8519-7353>Timothy C. Beers  <https://orcid.org/0000-0003-4573-6233>**References**

Alonso, A., Arribas, S., & Martínez-Roger, C. 1996, *A&A*, **313**, 873  
 Alonso, A., Arribas, S., & Martínez-Roger, C. 1999, *A&AS*, **140**, 261  
 Alvarez, R., & Plez, B. 1998, *A&A*, **330**, 1109  
 Anders, F., Chiappini, C., Santiago, B. X., et al. 2014, *A&A*, **564**, A115  
 Aoki, W., Beers, T. C., Christlieb, N., et al. 2007, *ApJ*, **655**, 492  
 Aoki, W., Beers, T. C., Lee, Y. S., et al. 2013, *AJ*, **145**, 13

Argast, D., Samland, M., Thielemann, F.-K., & Qian, Y.-Z. 2004, *A&A*, **416**, 997  
 Arnett, W. D. 1971, *ApJ*, **166**, 153  
 Asplund, M. 2005, *HiA*, **13**, 542  
 Asplund, M., Grevesse, N., Sauval, A. J., & Scott, P. 2009, *ARA&A*, **47**, 481  
 Audouze, J., & Silk, J. 1995, *ApJL*, **451**, L49  
 Baumüller, D., & Gehren, T. 1997, *A&A*, **325**, 1088  
 Bayo, A., Rodrigo, C., Barrado Y Navascués, D., et al. 2008, *A&A*, **492**, 277  
 Beers, T. C., & Christlieb, N. 2005, *ARA&A*, **43**, 531  
 Beers, T. C., Placco, V. M., Carollo, D., et al. 2017, *ApJ*, **835**, 81  
 Beers, T. C., Preston, G. W., & Shectman, S. A. 1985, *AJ*, **90**, 2089  
 Beers, T. C., Preston, G. W., & Shectman, S. A. 1992, *AJ*, **103**, 1987  
 Bergemann, M., & Cescutti, G. 2010, *A&A*, **522**, A9  
 Bonifacio, P., Caffau, E., Spite, M., et al. 2015, *A&A*, **579**, A28  
 Bonifacio, P., Molaro, P., Sivarani, T., et al. 2007, *A&A*, **462**, 851  
 Bonifacio, P., Spite, M., Cayrel, R., et al. 2009, *A&A*, **501**, 519  
 Bromm, V., Yoshida, N., Hernquist, L., & McKee, C. F. 2009, *Natur*, **459**, 49  
 Cameron, A. G. W., & Fowler, W. A. 1971, *ApJ*, **164**, 111  
 Carretta, E., Bragaglia, A., D'Orazi, V., Lucatello, S., & Gratton, R. G. 2010, *A&A*, **519**, A71  
 Carretta, E., Gratton, R., Cohen, J. G., Beers, T. C., & Christlieb, N. 2002, *AJ*, **124**, 481  
 Castelli, F., & Kurucz, R. L. 2004, arXiv:astro-ph/0405087  
 Cayrel de Strobel, G., & Spite, M. (ed.) 1988, in IAU Symp. 132, The Impact of very high S/N spectroscopy on stellar physics (Dordrecht: Kluwer)  
 Cayrel, R., Depagne, E., Spite, M., et al. 2004, *A&A*, **416**, 1117  
 Chiaki, G., Susa, H., & Hirano, S. 2018, *MNRAS*, **475**, 4378  
 Chiaki, G., Tominaga, N., & Nozawa, T. 2017, *MNRAS*, **472**, L115  
 Chiappini, C. 2013, *AN*, **334**, 595  
 Choplin, A., Maeder, A., Meynet, G., & Chiappini, C. 2016, *A&A*, **593**, A36  
 Christlieb, N. 2003, *RvMA*, **16**, 191  
 Coelho, P., Percival, S. M., & Salaris, M. 2011, *ApJ*, **734**, 72  
 Cooke, R. J., & Madau, P. 2014, *ApJ*, **791**, 116  
 Cowan, J. J., & Rose, W. K. 1977, *ApJ*, **212**, 149  
 de Laverny, P., Recio-Blanco, A., Worley, C. C., & Plez, B. 2012, *A&A*, **544**, A126  
 Denissenkov, P. A., & Herwig, F. 2004, *ApJ*, **612**, 1081  
 Drout, M. R., Piro, A. L., Shappee, B. J., et al. 2017, *Sci*, **358**, 1570  
 Eisenstein, D. J., Weinberg, D. H., Agol, E., et al. 2011, *AJ*, **142**, 72  
 Fernández-Alvar, E., Allende Prieto, C., Beers, T. C., et al. 2016, *A&A*, **593**, A28  
 Frebel, A., Christlieb, N., Norris, J. E., et al. 2006, *ApJ*, **652**, 1585  
 Frebel, A., & Norris, J. E. 2015, *ARA&A*, **53**, 631  
 Fulbright, J. P., Wyse, R. F. G., Ruchti, G. R., et al. 2010, *ApJL*, **724**, L104  
 García Pérez, A. E., Cunha, K., Shetrone, M., et al. 2013, *ApJL*, **767**, L9  
 Gratton, R., Sneden, C., & Carretta, E. 2004, *ARA&A*, **42**, 385  
 Gratton, R. G., Bonifacio, P., Bragaglia, A., et al. 2001, *A&A*, **369**, 87  
 Grevesse, N., Scott, P., Asplund, M., & Sauval, A. J. 2015, *A&A*, **573**, A27  
 Gustafsson, B., Edvardsson, B., Eriksson, K., et al. 2008, *A&A*, **486**, 951  
 Hampel, M., Stancliffe, R. J., Lugaro, M., & Meyer, B. S. 2016, *ApJ*, **831**, 171  
 Hansen, T. T., Andersen, J., Nordström, B., et al. 2016a, *A&A*, **588**, A3  
 Hansen, T. T., Andersen, J., Nordström, B., et al. 2016b, *A&A*, **586**, A160  
 Heger, A., & Woosley, S. E. 2002, *ApJ*, **567**, 532  
 Heger, A., & Woosley, S. E. 2010, *ApJ*, **724**, 341  
 Ivezić, Ž., Beers, T. C., & Jurić, M. 2012, *ARA&A*, **50**, 251  
 Johnson, J. A., Herwig, F., Beers, T. C., & Christlieb, N. 2007, *ApJ*, **658**, 1203  
 Kilpatrick, C. D., Foley, R. J., Kasen, D., et al. 2017, *Sci*, **358**, 1583  
 Lai, D. K., Bolte, M., Johnson, J. A., et al. 2008, *ApJ*, **681**, 1524  
 Lau, H. H. B., Stancliffe, R. J., & Tout, C. A. 2007, *MNRAS*, **378**, 563  
 Lee, Y. S., Beers, T. C., Kim, Y. K., et al. 2017, *ApJ*, **836**, 91  
 Lee, Y. S., Beers, T. C., Masseron, T., et al. 2013, *AJ*, **146**, 132  
 Li, H.-N., Zhao, G., Christlieb, N., et al. 2015, *ApJ*, **798**, 110  
 Lucatello, S., Tsangarides, S., Beers, T. C., et al. 2005, *ApJ*, **625**, 825  
 Maeder, A., & Meynet, G. 2015, *A&A*, **580**, A32  
 Maeder, A., Meynet, G., & Chiappini, C. 2015, *A&A*, **576**, A56  
 Masseron, T., Johnson, J. A., Lucatello, S., et al. 2012, *ApJ*, **751**, 14  
 Masseron, T., van Eck, S., Famaey, B., et al. 2006, *A&A*, **455**, 1059  
 Matsuno, T., Aoki, W., Beers, T. C., Lee, Y. S., & Honda, S. 2017, *AJ*, **154**, 52  
 McWilliam, A. 1998, *AJ*, **115**, 1640  
 McWilliam, A., Preston, G. W., Sneden, C., & Searle, L. 1995, *AJ*, **109**, 2757  
 Mészáros, S., Martell, S. L., Shetrone, M., et al. 2015, *AJ*, **149**, 153  
 Meynet, G., Ekström, S., & Maeder, A. 2006, *A&A*, **447**, 623  
 Meynet, G., Hirschi, R., Ekström, S., et al. 2010, *A&A*, **521**, A30  
 Nakamura, T., Umeda, H., Nomoto, K., Thielemann, F.-K., & Burrows, A. 1999, *ApJ*, **517**, 193



- Nishimura, N., Takiwaki, T., & Thielemann, F.-K. 2015, *ApJ*, **810**, 109
- Nomoto, K., Kobayashi, C., & Tominaga, N. 2013, *ARA&A*, **51**, 457
- Paegert, M., Stassun, K. G., De Lee, N., et al. 2015, *AJ*, **149**, 186
- Peterson, R. C. 1976, *ApJ*, **206**, 800
- Piau, L., Beers, T. C., Balsara, D. S., et al. 2006, *ApJ*, **653**, 300
- Pinsonneault, M. H., Walker, T. P., Steigman, G., & Narayanan, V. K. 1999, *ApJ*, **527**, 180
- Placco, V. M., Frebel, A., Beers, T. C., et al. 2016, *ApJ*, **833**, 21
- Placco, V. M., Frebel, A., Beers, T. C., & Stancliffe, R. J. 2014, *ApJ*, **797**, 21
- Plez, B., & Cohen, J. G. 2005, *A&A*, **434**, 1117
- Pols, O. R., Izzard, R. G., Glebbeek, E., & Stancliffe, R. J. 2009, *PASA*, **26**, 327
- Pols, O. R., Izzard, R. G., Stancliffe, R. J., & Glebbeek, E. 2012, *A&A*, **547**, A76
- Qian, Y.-Z., & Wasserburg, G. J. 2002, *ApJ*, **567**, 515
- Ramírez, I., & Meléndez, J. 2005, *ApJ*, **626**, 465
- Ryan, S. G., Norris, J. E., & Beers, T. C. 1996, *ApJ*, **471**, 254
- Scott, P., Asplund, M., Grevesse, N., Bergemann, M., & Sauval, A. J. 2015a, *A&A*, **573**, A26
- Scott, P., Grevesse, N., Asplund, M., et al. 2015b, *A&A*, **573**, A25
- Shapsee, B. J., Simon, J. D., Drout, M. R., et al. 2017, *Sci*, **358**, 1574
- Sharma, M., Theuns, T., Frenk, C., & Cooke, R. J. 2018, *MNRAS*, **473**, 984
- Shetrone, M. D. 1996, in ASP Conf. Ser. 92, Formation of the Galactic Halo... Inside and Out, ed. H. L. Morrison & A. Sarajedini (San Francisco, CA: ASP), 383
- Shi, J. R., Takada-Hidai, M., Takeda, Y., et al. 2012, *ApJ*, **755**, 36
- Sivarani, T., Beers, T. C., Bonifacio, P., et al. 2006, *A&A*, **459**, 125
- Smith, B. D., Wise, J. H., O'Shea, B. W., Norman, M. L., & Khochfar, S. 2015, *MNRAS*, **452**, 2822
- Spite, F., & Spite, M. 1982, *A&A*, **115**, 357
- Spite, M., Caffau, E., Bonifacio, P., et al. 2013, *A&A*, **552**, A107
- Spite, M., Cayrel, R., Hill, V., et al. 2006, *A&A*, **455**, 291
- Spite, M., Cayrel, R., Plez, B., et al. 2005, *A&A*, **430**, 655
- Starkenburger, E., Shetrone, M. D., McConnachie, A. W., & Venn, K. A. 2014, *MNRAS*, **441**, 1217
- Steigman, G. 2005, *PhST*, **121**, 142
- Suda, T., Katsuta, Y., Yamada, S., et al. 2008, *PASJ*, **60**, 1159
- Suda, T., Komiya, Y., Yamada, S., et al. 2012, in AGB Evolution and Nucleosynthesis at Low-metallicity Constrained by the Star Formation History of our Galaxy, ed. J. Lattanzio, A. Karakas, & G. Dracoulis (Trieste: SISSA), 234
- Susmitha Rani, A., Sivarani, T., Beers, T. C., et al. 2016, *MNRAS*, **458**, 2648
- Tominaga, N., Iwamoto, N., & Nomoto, K. 2014, *ApJ*, **785**, 98
- Truran, J. W., & Arnett, W. D. 1971, *Ap&SS*, **11**, 430
- Umeda, H., & Nomoto, K. 2003, *Natur*, **422**, 871
- Umeda, H., & Nomoto, K. 2005, *ApJ*, **619**, 427
- Umeda, H., Nomoto, K., & Nakamura, T. 2000, in The First Stars, ed. A. Weiss, T. G. Abel, & V. Hill (Berlin: Springer-Verlag), 150
- Winteler, C., Käppeli, R., Peregó, A., et al. 2012, *ApJL*, **750**, L22
- Woosley, S. E., & Weaver, T. A. 1986, *ARA&A*, **24**, 205
- Wright, J. T., & Howard, A. W. 2009, *ApJS*, **182**, 205
- Yoon, J., Beers, T. C., Placco, V. M., et al. 2016, *ApJ*, **833**, 20
- Zhao, G., Zhao, Y., Chu, Y., Jing, Y., & Deng, L. 2012, arxiv:1206.3569